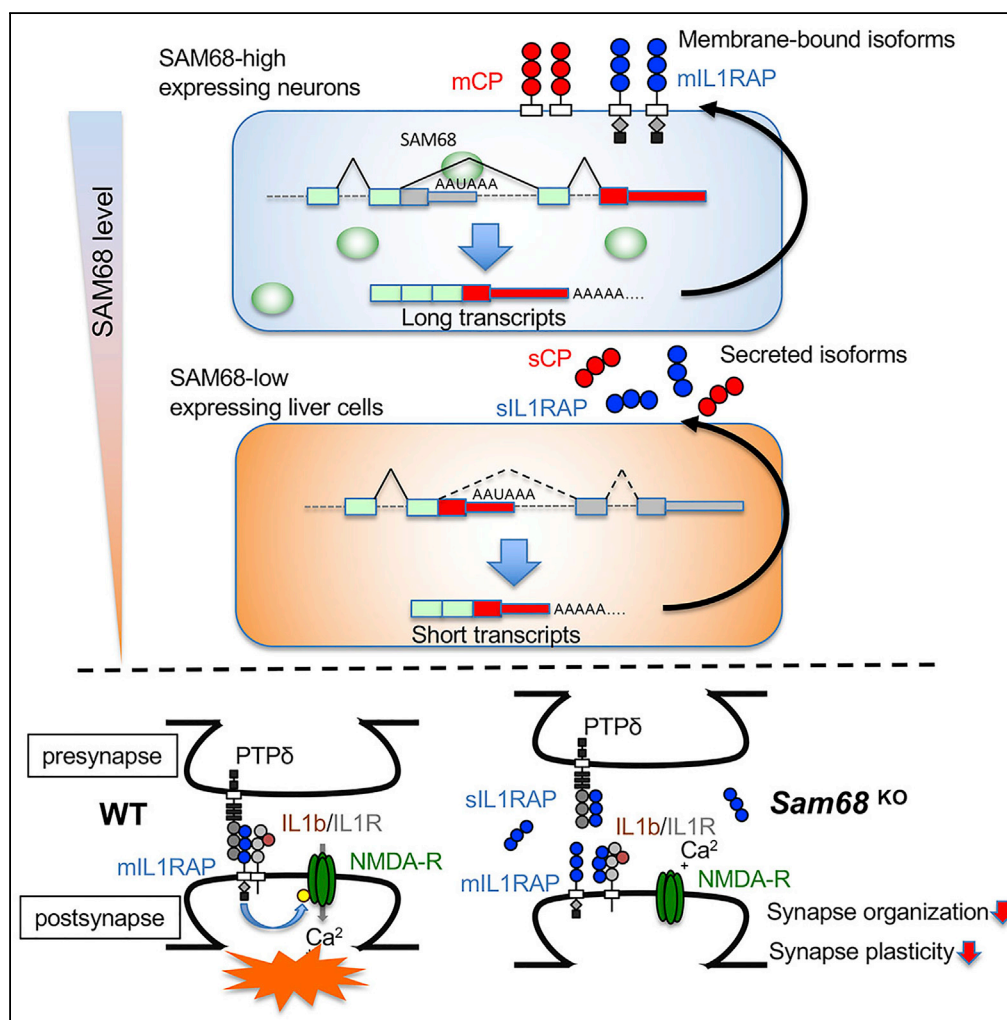


Article

SAM68-Specific Splicing Is Required for Proper Selection of Alternative 3' UTR Isoforms in the Nervous System



Yoko Iijima,
Masami Tanaka,
Satoko Suzuki, ...,
Masato Ohtsuka,
Peter Scheiffele,
Takatoshi Iijima

takatoshi.iijima@tokai-u.jp

HIGHLIGHTS

SAM68 and the related protein SLM1 exhibit distinct alternative splicing activity

SAM68 specifically controls 3' UTR selection of multiple neuronal genes

Proper 3' UTR selection is necessary for IL1RAP neuronal function

Neuronal expression of SAM68 requires proper 3' UTR selection in the nervous system

DATA AND CODE

AVAILABILITY

GSE110258

Iijima et al., iScience 22, 318–335
December 20, 2019 © 2019
The Author(s).
<https://doi.org/10.1016/j.isci.2019.11.028>



Article

SAM68-Specific Splicing Is Required for Proper Selection of Alternative 3' UTR Isoforms in the Nervous System

Yoko Iijima,^{1,2,5} Masami Tanaka,^{1,5} Satoko Suzuki,^{1,5} David Hauser,³ Masayuki Tanaka,⁴ Chisa Okada,⁴ Masatoshi Ito,⁴ Noriko Ayukawa,¹ Yuji Sato,^{1,2} Masato Ohtsuka,² Peter Scheiffele,³ and Takatoshi Iijima^{1,2,6,*}

SUMMARY

Neuronal alternative splicing is a core mechanism for functional diversification. We previously found that STAR family proteins (SAM68, SLM1, SLM2) regulate spatiotemporal alternative splicing in the nervous system. However, the whole aspect of alternative splicing programs by STARs remains unclear. Here, we performed a transcriptomic analysis using SAM68 knockout and SAM68/SLM1 double-knockout midbrains. We revealed different alternative splicing activity between SAM68 and SLM1; SAM68 preferentially targets alternative 3' UTR exons. SAM68 knockout causes a long-to-short isoform switch of a number of neuronal targets through the alteration in alternative last exon (ALE) selection or alternative polyadenylation. The altered ALE usage of a novel target, interleukin 1 receptor accessory protein (*Il1rap*), results in remarkable conversion from a membrane-bound type to a secreted type in *Sam68*^{KO} brains. Proper ALE selection is necessary for IL1RAP neuronal function. Thus the SAM68-specific splicing program provides a mechanism for neuronal selection of alternative 3' UTR isoforms.

INTRODUCTION

Alternative pre-mRNA splicing is a powerful mechanism that generates molecular diversity from a limited number of genes and is therefore thought to be essential for biological complexity and diversity in mammals. In particular, the regulation is highly dynamic and complex in the central nervous system (CNS) (Barbosa-Morais et al., 2012; Merkin et al., 2012). Alternative splicing decisions are known to be dynamically switched during neural development (Kalsotra and Cooper, 2011; Vuong et al., 2016) and show distinct patterns in a neuronal tissue- or cell type-specific manner (Iijima et al., 2016; Nguyen et al., 2016; Li et al., 2007; Raj and Blencowe, 2015). Furthermore, neuronal activity modulates alternative splicing of neural genes via Ca²⁺-dependent signaling pathways (Razanau and Xie, 2013). Thus, neuronal alternative splicing is dynamically controlled in a spatiotemporal manner, which likely contributes to brain function complexity and diversity (Li et al., 2007; Raj and Blencowe, 2015). However, the RNA regulatory mechanisms underlying spatiotemporal and dynamic alternative splicing in neurons are only now being uncovered.

Neuronal alternative splicing is dynamically exerted by regulatory activity and unique expression patterns of RNA-binding proteins (RBPs). We previously identified SAM68 (Src-associated in mitosis of 68-kDa protein, *khdrb1*) as a critical regulator of neuronal activity-regulated alternative splicing (Iijima et al., 2011). Moreover, two related proteins, SLM1 and SLM2 (SAM-like molecule 1 and 2), have been implicated in neuronal cell-type-specific splicing (Ehrmann et al., 2013; Iijima et al., 2014; Nguyen et al., 2016). SAM68, SLM1, and SLM2 belong to the STAR (signal transduction and activation of RNA) family of proteins, which share 70%–80% of amino acid sequence identities in their KH-type RNA-binding domains (Di Fruscio et al., 1999). Important targets of SAM68, SLM1, and SLM2 are the mRNAs encoding Neurexin (*Nrxn*) proteins (Iijima et al., 2016). Neurexins are synaptic cell surface receptors extensively regulated at alternative splicing level (Missler and Sudhof, 1998). All three STAR family proteins induce skipping of exon 20 at the *Nrxn* alternatively spliced segment 4 (AS4). The splicing decision at AS4 is critical for differential interactions with several ligands that are essential mediators of synaptic properties, including neuroligins, leucine-rich repeat proteins, and the Cbln1-GluD2 complex (Baudouin and Scheiffele, 2010; Boucard et al., 2005; Ko et al., 2009; Krueger et al., 2012; Matsuda and Yuzaki, 2011; Uemura et al., 2010). Indeed, the *Nrxn* AS4 is particularly important for synaptic strength and plasticity regulation (Aoto et al., 2013; Traunmuller et al., 2016), which is dynamically controlled by STAR family proteins in neuronal

¹Tokai University Institute of Innovative Science and Technology, 143 Shimokasuya, Isehara City, Kanagawa 259-1193, Japan

²Department of Molecular Life Science, Division of Basic Medical Science and Molecular Medicine, School of Medicine, Tokai University, 143, Shimokasuya, Isehara, Kanagawa 259-1193, Japan

³Biozentrum, University of Basel, Klingelbergstrasse 50-70, Basel 4056, Switzerland

⁴The Support Center for Medical Research and Education, Tokai University, 143 Shimokasuya, Isehara City, Kanagawa 259-1193, Japan

⁵These authors contributed equally

⁶Lead Contact

*Correspondence: takatoshi.ijima@tokai-u.jp
<https://doi.org/10.1016/j.isci.2019.11.028>



activity- and cell-type-specific fashions (Ehrmann et al., 2013; Iijima et al., 2011, 2014; Nguyen et al., 2016; Traunmuller et al., 2016).

Several groups have previously identified additional substrates for SAM68 and SLM2 (Chawla et al., 2009; Ehrmann et al., 2013, 2016; Huot et al., 2012; La Rosa et al., 2016; Traunmuller et al., 2016). Knockout mice of SAM68, SLM1, and SLM2 exhibit several morphological and functional defects in adult brains (Ehrmann et al., 2016; Iijima et al., 2011, 2014; Lukong and Richard, 2008; Traunmuller et al., 2016). We previously found that *Sam68* and *Slm1*^{KO} mice particularly have cerebellar malformation and motor deficits (Iijima et al., 2011, 2014). Nevertheless, most neuronal functions of STAR family proteins in the mature brain remain unresolved. However, given that SAM68 and SLM1 are widely expressed in the brain throughout life, spatiotemporal regulation of alternative splicing by SAM68/SLM1 could play a critical role in multiple aspects of neuronal development, differentiation, and function. Thus, the recent findings pave the way to uncover and characterize novel targets for spatiotemporal alternative splicing programs by SAM68/SLM1 in the nervous system. Here we reveal that SAM68 shapes neuronal diversity of alternative 3' UTR isoforms and demonstrate the critical role of the SAM68 splicing program in the proper 3' UTR selection.

RESULTS

Characterization of SAM68/SLM1-Dependent Alternative Splicing Programs

To decipher alternative splicing programs encoded by SAM68 and SLM1 proteins, we attempted to locate new candidate RNA substrates by microarray-based screening using SAM68/SLM1 knockout mice. We utilized the exon array on the primary experiments, the dataset was validated by RT-qPCR, and the altered exons were further confirmed by RNA sequencing (RNA-seq). We previously showed that SLM1 protein acts as a heteromeric complex with SAM68 in co-expressing neurons (Iijima et al., 2014). Given that STARs share 70%–80% of amino acid sequence identity in their RNA-binding domains (Di Fruscio et al., 1999), it is expected that SAM68 would share a significant amount of RNA substrates with SLM1 with functional redundancy. Therefore, for the initial transcriptomic analysis, we attempted to identify candidate RNA substrates in the midbrain of both SAM68/SLM1 double-knockout (*Sam68/Slm1*^{DKO}) mice and SLM1 single-knockout (*Slm1*^{KO}) mice. We focused this analysis on the midbrain because this area is a site of prominent co-expression of SAM68 and SLM1. Initially, we compared the levels of gene expression between wild-type (WT), *Slm1*^{KO}, and *Sam68/Slm1*^{DKO} mice. A scatterplot showed that the gene expression profiles of *Slm1*^{KO} and *Sam68/Slm1*^{DKO} mice were highly similar to those of WT mice (correlated efficiency: 0.996–0.997) (Figure S1A), indicating that knockout of SAM68 and/or SLM1 did not significantly influence overall transcript levels. In fact, the volcano plots showed that there were only 10–12 genes that are significantly altered in both *Sam68/Slm1*^{DKO} and *Slm1*^{KO} mice compared with WT (corrected p values < 0.05; threshold set: fold change [FC] ≥ 2.0) (Figure S1B, and Table S1). Validation by RT-qPCR showed that the gene alterations are partially shared between both genotypes (Figure S1C), but others are unique for either SAM68 or SLM1 (Figure S1D). However, *Slm1* transcripts were not listed in the altered genes on the exon array. Although we previously confirmed that SLM1 protein is completely lacking in *Slm1*^{KO} mice (Iijima et al., 2014), the RNA-seq data exhibited that the transcripts lacking exon 2 remain expressed (data not shown). That is why *Slm1* transcripts were not listed in the downregulated genes. Reportedly, SAM68 has multiple functions on RNA metabolism, and a multitude of RNA substrates including non-coding RNAs have been identified using other approaches (Li et al., 2017; Sanchez-Jimenez and Sanchez-Margalet, 2013; Vogel and Richard, 2012). Therefore the very modest number of transcriptomic changes identified in our sample was surprising. The results were largely confirmed by RNA-seq analysis in *Sam68/Slm1*^{DKO} mice (cor. efficiency: 0.986) (Figure S2A). Nevertheless, our results suggest that, even in *Slm1/Sam68* double-knockout mice, the effect on total transcript levels is likely to be only minor in the mouse midbrain.

We next examined exon alteration between WT, *Slm1*^{KO}, and *Sam68/Slm1*^{DKO} mice. We observed that 122 and 172 exons were altered by more than 2.4-fold in *Slm1*^{KO} and *Sam68/Slm1*^{DKO} mice, respectively (Figure 1A). Given that the whole gene expression profiles were almost unchanged (Figure S1), the majority of the exon alterations were likely due to the change in splicing events. We then compared the altered profiles at the exon level between *Slm1*^{KO} and *Sam68/Slm1*^{DKO} midbrains. The Venn diagram exhibited that 66 of 228 exons overlapped between the genotypes. We also found that 106 exons were altered only in *Sam68/Slm1*^{DKO} mice (Figure 1B). These exons are likely to contain SAM68-specific targets. We also observed that 56 exons were altered only in *Slm1*^{KO} mice. Indeed, given our previous finding that splicing activity of *Nrxn3* exon20 is quite opposite between the two proteins (Iijima et al., 2014), these could also include exons that are regulated differentially between SAM68 and SLM1. Gene ontology (GO) analysis of the

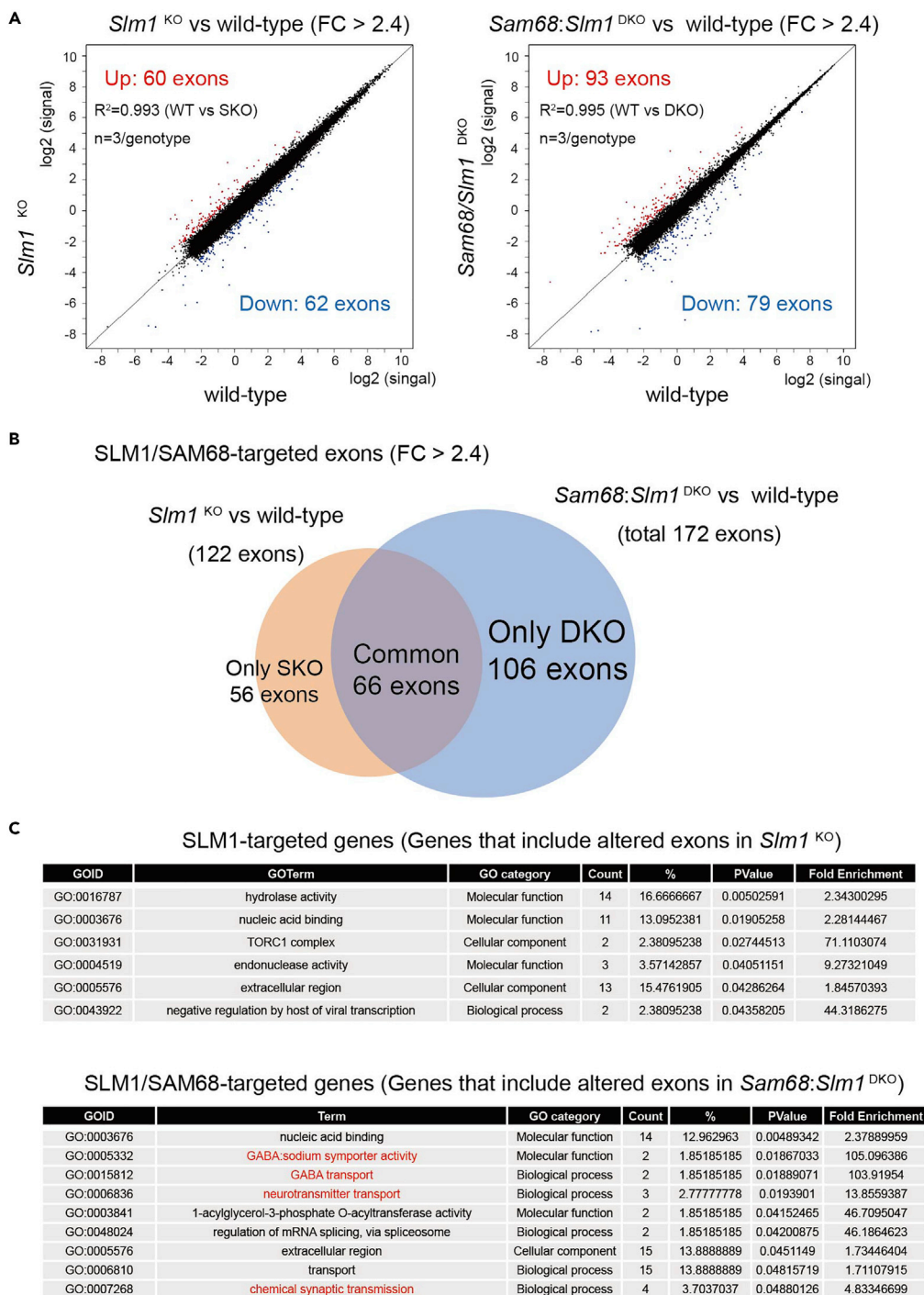


Figure 1. Comprehensive Comparison of Altered Exon Profiles between *Slm1*^{KO} and *Sam68/Slm1*^{DKO} Mice

Total RNAs from midbrains of WT, *Slm1*^{KO}, and *Sam68/Slm1*^{DKO} mice were subjected to data analyses on exon array (Agilent, Sure Print G3 Mouse Exon Microarray 2x400 K) (n = 3 animals/genotype).

(A) Scatterplots showing fold change for exons (*Slm1*^{KO} versus WT, *Sam68/Slm1*^{DKO} versus WT) (total 122 and 172 exons, respectively; threshold set: FC ≥ 2.4, raw probe signal intensity ≥ 100 in either of the two genotypes, normalized gene expression > -3 in either of the two genotypes) (n = 3 per genotype) (red and blue dots).

(B) Venn diagram showing the numbers of altered exons (total 228 exons; threshold set: FC ≥ 2.4, raw probe signal intensity ≥ 100 in either of the two genotypes, normalized gene expression > -3) in both *Slm1*^{KO} and *Sam68/Slm1*^{DKO} mice.

Figure 1. Continued

(C) Comparison of altered exons by GO analysis between *Slm1*^{KO} and *Sam68/Slm1*^{DKO} mice. Genes that encode altered exons (FC ≥ 2.4) shown in (A) (*Slm1*^{KO}: 89 genes; *Sam68/Slm1*^{DKO}: 112 genes) were subjected to GO analysis. Enrichment was thresholded by p value (p < 0.05). Red represents the neuronal terms.

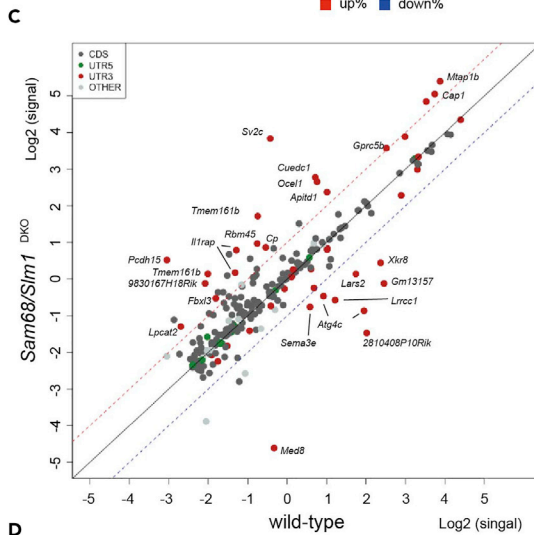
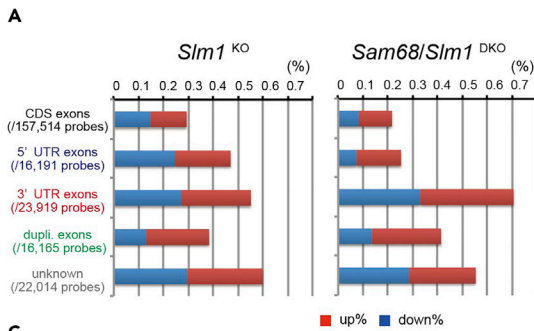
altered exons in each genotype showed that major subsets were enriched for similar terms, but those in *Sam68/Slm1*^{DKO} mice were much more enriched for the neuronal terms (Figure 1C, red terms). Therefore, these results imply that SAM68 and SLM1 encode overlapping but distinct alternative splicing programs.

The SAM68-Specific Splicing Program Preferentially Regulates Alternative 3' UTR Exons of Neuronal Genes

To further pursue the potential difference in the splicing program between SAM68 and SLM1, we then classified significantly altered exons into five categories (coding sequence [CDS], 5' untranslated region [5' UTR], 3' untranslated region [3' UTR], duplicated [containing both CDS and UTR], and unknown [not annotated in refseq] exons), and compared the relative percentage of each altered exon between *Slm1*^{KO} and *Sam68/Slm1*^{DKO} mice. Interestingly, we noticed that there was a remarkable difference in the pattern of the exon alteration between *Slm1*^{KO} and *Sam68/Slm1*^{DKO} mice; 3' UTR exons were preferentially altered in *Sam68/Slm1*^{DKO} mice (Figure 2A), although RNA-seq data in *Sam68/Slm1*^{DKO} mice showed that these exon alterations largely included all alternative exon events (i.e., cassette exons, mutually exclusive exons, alternative 5' splice site, alternative 3' splice site, and retained introns) (Figure S2B). Indeed, 3' UTR exons were frequently observed in the top lists of significantly altered exons in *Sam68/Slm1*^{DKO} mice (Figure 2B). We listed 35 genes whose 3' UTR exons were significantly altered (threshold set: FC > 2.4, p < 0.05) (Table S2). Twenty of 35 genes were unique for *Sam68/Slm1*^{DKO} mice. Importantly, arranged scatterplots of all exons (251 exons) in 35 genes showed that the alteration in 3' UTR exons likely did not follow the change in their neighboring coding exons within their encoding genes (Figure 2C), indicating a specific alteration in alternative 3' UTR isoform choice of these genes.

Interestingly, GO analyses of the altered 3' UTR exons in *Sam68/Slm1*^{DKO} mice predicted that significant numbers of these targets might include transcripts encoding transmembrane or secreted proteins with neuronal function (Figure 2D). Intriguing examples were exon 8b of *Il1rap* (interleukin 1 receptor accessory protein, synaptic adhesion protein), exon 26b of *Pcdh15* (protocadherin-15, cell adhesion protein that plays an essential role in maintenance of normal retinal and cochlear function), exon 19 of *Cp* (ceruloplasmin, iron transporter), and exon 4b of *Gla3* (glycine receptor alpha 3, glycinergic ion channel) (see Figure 2C). Indeed, RNA-seq analysis showed that the proximal 3' UTR exons of these transcripts were markedly included in *Sam68/Slm1*^{DKO} mice, whereas these were almost excluded in WT mice (Figures 2E and S2C), resulting in a long-to-short isoform switch of several neuronal targets through alteration in alternative last exon (ALE) selection in *Sam68/Slm1*^{DKO} mice. In addition, because preferential alteration in 3' UTR exons occurred in *Sam68/Slm1*^{DKO}, but not particularly in *Slm1*^{KO} mice (Figures 2A and 2B), we hypothesized that the aberrant choice of alternative 3' UTR isoforms was largely caused by the single-knockout effect of SAM68. To clarify the possibility, the altered 3' UTR exon events observed in the exon array were validated in *Sam68*^{KO}, *Slm1*^{KO}, and *Slm2* mutant (*Slm2*^{MT}) brains separately by RT-qPCR analysis (Figure 3). *Slm2*^{MT} mice expressed SLM2 protein that lacks a first QUA domain (Figure S3), which results in a significant reduction in SLM2 activity toward alternative splicing of *Nrxn* AS4, a major SLM2 target in the brain (Figures S3E and S3F). In this analysis, we focused on eight genes (*Il1rap*, *Cp*, *Pcdh15*, *Lrrcc1*, *Pcdh17*, *Dlgap1*, *Sema3a*, and *Fbxl3*) observed only in *Sam68/Slm1*^{DKO} on the exon array. The RT-qPCR analyses revealed that these exon alterations did not occur in *Slm1*^{KO} and *Slm2*^{MT} mice, except for *Fbxl3*, and were specifically caused by single loss of *Sam68* (Figure 3). The *Sam68*^{KO}-specific alternation included all three types of alternative 3' UTR splicing events (ALE type [Figure 3A], ALE type with alternative 5' splice site [Figure 3B], and alternative polyadenylation type [APA] [Figure 3C]). Thus, these data show that the SAM68-specific splicing program controls alternative 3' UTR isoform selection.

To further investigate the ALE choice by SAM68, we focused on alternative splicing of *Il1rap* (ALE with alternative 5' splice site), *Pcdh15* (ALE), *Cp* (ALE), and *Gla3* (ALE). The RT-qPCR analyses revealed that short-form (SF) variants of *Il1rap*, *Pcdh15*, *Cp*, and *Gla3* including proximal 3' UTR exons were dramatically increased in the midbrain of *Sam68*^{KO} and *Sam68/Slm1*^{DKO} mice, whereas the long-form (LF) variant was reciprocally reduced (Figures 4A–4D, S4, and S5A). Notably, whereas >90% of *Il1rap* transcripts account for an LF variant in WT mice, >50% of these transcripts were occupied by the atypical SF variant in



D SLM1/SAM68-targeted genes (including 3' UTR exons)

Keyword category

Enrichment terms	Category	Count	%Count	P-value	Fold enrichment
Secreted	Keywords	11	20.370	0.005	2.742
Pyroglutamate carboxylic acid	Keywords	3	5.555	0.008	21.356
Transmembrane helix	Keywords	24	44.444	0.033	1.453
Transmembrane	Keywords	24	44.444	0.034	1.449

B Up

Genes	Fold change (DKO/WT)	Fold change (SKO/WT)	P-value (DKO vs WT)	P-value (SKO vs WT)	P-value (DKO vs SKO)	exon type (No.)
<i>Sv2c</i>	19.21799811	11.47861481	**	*	n.s.	3UTR (exon13)
<i>Pcdh15</i>	11.63396645	-1.326714359	***	n.s.	**	3UTR (exon27)
<i>Gm13251</i>	6.62876188	8.613835443	**	**	n.s.	5UTR (exon2)
<i>Sv2c</i>	4.468406682	3.420905002	*	n.s.	n.s.	3UTR (exon13)
<i>Btd9</i>	4.279855119	3.183277651	*	n.s.	n.s.	CDS (exon5)
<i>Il1rap</i>	4.201840879	-1.2324068	**	n.s.	*	3UTR (exon8)
<i>Cuedc1</i>	4.101905127	1.472331452	**	n.s.	n.s.	3UTR (exon8)
<i>Wdr89</i>	3.961188022	3.310153452	**	***	n.s.	5UTR (exon1)
<i>9830167H18Rik</i>	3.863113508	3.217461202	**	*	n.s.	3UTR (exon1)
<i>Hyl</i>	3.473191067	3.099385614	***	*	n.s.	CDS (exon2)
<i>Cd6</i>	3.428037796	3.324217805	**	***	n.s.	CDS (exon2)
<i>2010315B03Rik</i>	3.37291727	1.243075665	**	n.s.	n.s.	CDS (exon1)
<i>Btd9</i>	3.35011092	2.773946692	*	*	n.s.	CDS (exon6)
<i>Rbm45</i>	3.251207734	3.431434314	**	*	n.s.	3UTR (exon10)
<i>Gm3435</i>	2.899916955	1.800376073	*	n.s.	n.s.	5UTR (exon1)
<i>Mtap1b</i>	2.86424072	1.988024592	*	n.s.	n.s.	3UTR (exon1)
<i>Tmem161b</i>	2.833448128	1.62400952	*	n.s.	n.s.	3UTR (exon12)
<i>LOC100048774</i>	2.786181299	2.644552381	**	***	n.s.	CDS (exon4)
<i>Ddr1</i>	2.710271328	2.995206145	*	n.s.	n.s.	CDS (exon13)
<i>Btd9</i>	2.679381312	2.350160108	*	n.s.	n.s.	CDS (exon7)
<i>Sema3e</i>	-2.548743496	-1.302671331	*	n.s.	n.s.	3UTR (exon17)
<i>Tatdn1</i>	-2.564295311	-1.154296454	**	n.s.	n.s.	CDS (exon3)
<i>Fyco1</i>	-2.577662592	-2.09108622	**	n.s.	n.s.	CDS (exon3)
<i>Atg4c</i>	-2.629483295	-3.782160938	*	**	n.s.	3UTR (exon11)
<i>Gm7120</i>	-2.802704197	-1.798714433	*	n.s.	n.s.	3UTR (exon3)
<i>Fyco1</i>	-2.826211549	-2.23775541	***	n.s.	n.s.	CDS (exon2)
<i>2810408P10Rik</i>	-3.039711705	-3.531038921	**	**	n.s.	CDS (exon1)
<i>Lars2</i>	-3.089801598	-1.608820741	***	n.s.	n.s.	3UTR (exon22)
<i>Gtra3</i>	-3.130726501	-1.035154035	*	n.s.	*	CDS (exon9)
<i>Cbr4</i>	-3.198202653	-3.19868017	*	*	n.s.	5UTR (exon1)
<i>Fyco1</i>	-3.482509235	-1.766675706	**	n.s.	n.s.	CDS (exon16)
<i>Lrrcc1</i>	-3.490191879	-1.376675019	**	n.s.	**	3UTR (exon19)
<i>Cp</i>	-3.633804946	-1.498397738	*	n.s.	n.s.	CDS+3UTR (exon19)
<i>Xkr8</i>	-3.8737646	-4.722714434	**	***	n.s.	3UTR (exon1)
<i>Sacm1l</i>	-5.981299871	-2.249475944	**	n.s.	n.s.	CDS (exon15)
<i>Gm13157</i>	-6.057746125	-7.282504301	***	*	n.s.	3UTR (exon1)
<i>Atg4c</i>	-6.992298495	-6.955490808	*	*	n.s.	3UTR (exon11)
<i>2810408P10Rik</i>	-11.49981593	-12.52405689	**	***	n.s.	3UTR (exon2)
<i>Med8</i>	-19.58043583	-25.42719369	**	**	n.s.	3UTR (exon7)
<i>Zbtb8os</i>	-52.20253689	-16.3266985	**	*	n.s.	CDS (exon5)

down

GO-enriched terms

GOID	Term	GO category	Count	%	P-value	Fold enrichment
GO:0005576	extracellular region	Cellular component	19	20.652	2.27E-04	2.599
GO:0007268	chemical synaptic transmission	Biological process	5	5.434	0.005	7.103
GO:0005184	neuropeptide hormone activity	Molecular function	3	3.261	0.006	25.066
GO:0006836	neurotransmitter transport	Biological process	3	3.261	0.014	16.291
GO:0032403	protein complex binding	Molecular function	6	6.522	0.015	4.061
GO:0015812	GABA transport	Biological process	2	2.174	0.016	122.175
GO:0005332	GABA:sodium symporter activity	Molecular function	2	2.174	0.016	121.152
GO:0008654	phospholipid biosynthetic process	Biological process	3	3.261	0.024	12.424
GO:0003841	1-acylglycerol-3-phosphate O-acyltransferase activity	Molecular function	2	2.174	0.036	53.845

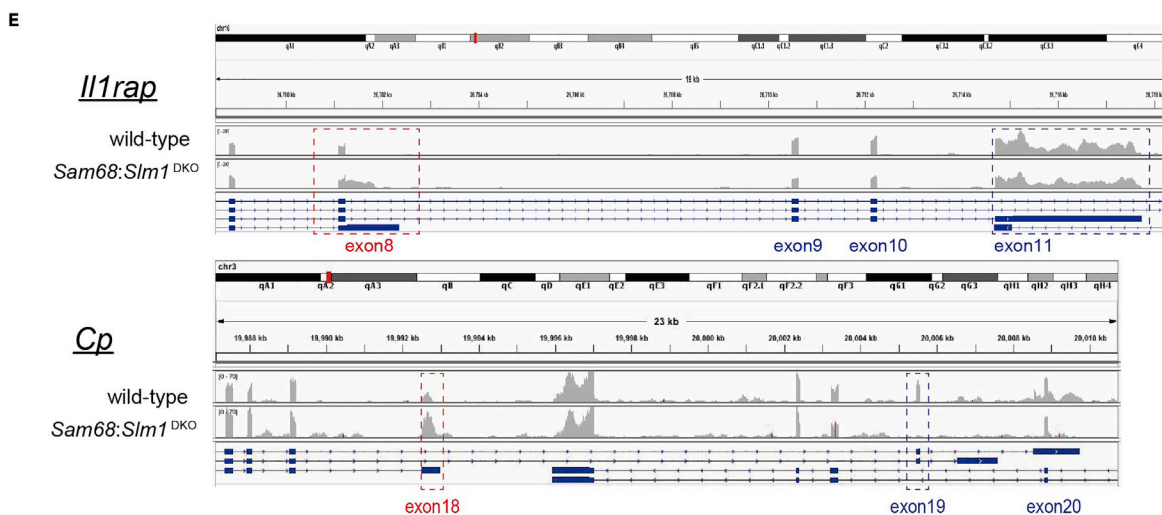


Figure 2. Altered 3' UTR Exon Events Of Neuronal Genes in *Sam68/Slm1*^{DKO} Brains

(A) Classification of exons altered in *Slm1*^{KO} and *Sam68/Slm1*^{DKO} mice on exon array datasets. Exons are classified into the following five categories: CDS, 5' UTR, 3' UTR, duplicated, and unknown exons. (threshold set: raw probe signal intensity ≥ 100 in either of the two genotypes, FC ≥ 2.0). The x axis represents the percentage of altered exons per classified exon. Annotation was referenced on Mouse July 2007 (NCBI37/mm9).

(B) The list of top 20 list exons that were significantly increased or decreased in *Sam68/Slm1*^{DKO} midbrains (excluding unknown genes and genes including exons altered at the gene level) (threshold set: FC ≥ 2.4 , raw probe signal intensity ≥ 100 in either of the two genotypes, normalized gene expression > -3 in either of the two genotypes, $p < 0.05$ [compared to WT]). SKO: *Slm1*^{KO}; DKO: *Sam68/Slm1*^{DKO}.

(C) Arranged scatterplots of all exons (total 251 exons) in 35 genes that include the significantly altered 3' UTR exons in *Sam68/Slm1*^{DKO} mice. CDS, 5' UTR, 3' UTR, duplicated, and unknown exons.

(D) GO analyses of genes that include altered 3' UTR exons in *Sam68/Slm1*^{DKO} mice; 78 genes that include significantly altered 3' UTR exons (FC ≥ 2.0 , $p < 0.05$) were subjected to GO analysis. Enrichment was thresholded by p value ($p < 0.05$). Keyword category (left). GO-enriched terms (right). Red represents the neuronal terms.

(E) Aberrant 3' UTR exon selection of the representative genes, *Il1rap* and *Cp*, in *Sam68/Slm1*^{DKO} brains shown by RNA-seq (Illumina Hiseq). The alignment of RNA-seq was based on the UCSC genome browser Mouse NCBI37/mm10 assembly.

Sam68^{KO} and *Sam68/Slm1*^{DKO} mice (Figure 4C). By contrast, knockout of *Slm1* did not affect any isoform levels of these transcripts and did not have additive effects with loss of SAM68 (Figures 4A–4D and S4). In addition, the isoform alteration in other analyzed transcripts as shown in Figure 3 (*Lrrcc1*, *Pcdh17*, *Dlgap1*, *sema3e*, and *Fbxl3*) also had no additive effects with the double knockout (Figures S5B–S5D). Thus, we confirmed that these ALE selections are specifically controlled by SAM68. Interestingly, at the protein level, inclusion of *Il1rap* exon 8b, *Pcdh15* exon 26b, *Cp* exon 17, and *Gira3* exon 4b results in production of soluble forms, lacking transmembrane domains or glycosylphosphatidylinositol anchor (Figure S6A). Indeed, when these soluble-form variants were expressed in HEK293T cells, significant amounts of protein products were detected in the cultured medium (Figure S6B). The majority of *Il1rap*, *Pcdh15*, *Cp*, and *Gira3* transcripts are LF variants encoding transmembrane proteins in WT brains (Figures 4A–4D and S4). There are three ALEs in *Il1rap*, which produce two transmembrane (isoforms 1 and 3) and one soluble isoform (isoform 2) (Figure 4E, illustration). Consistent with the altered ALE selection at the transcript level, protein analysis by parallel reaction monitoring exhibits significant reduction in transmembrane protein isoform 1 in *Sam68*^{KO} brains relative to overall *Il1rap* protein levels (Isoform 1, 2, 3 [total]) (Figure 4E). These results indicate that aberrant ALE selection of these transcripts in *Sam68*^{KO} causes marked conversion into atypical secreted type of proteins in the nervous system.

Soluble IL1RAP Influences Synaptogenic Signaling through Transsynaptic IL1RAP-PTP δ Interaction

Our data indicated that single loss of SAM68 caused aberrant ALE selection of *Il1rap*, *Pcdh15*, and *Gira3* in *Sam68*^{KO}, resulting in marked conversion into atypical secreted type of proteins in the nervous system. Therefore, we then tested the influence of short/secreted isoforms on neuronal functions. A previous study revealed that IL1RAP and the paralog IL1RAP-like 1 (IL1RAP-L1) organize excitatory synapses through transsynaptic interaction with the protein tyrosine phosphatase δ (PTP δ), a member of the presynaptic cell adhesion molecule, in the nervous system (Yoshida et al., 2011, 2012) (Figure 5A). We examined the mRNA expression of *Il1rap* and of the related molecules in various brain regions and the developing cortex. The transcripts were ubiquitously expressed in whole brain tissues and throughout development (Figures S7A and S7B). In addition, ALE choice of *Il1rap* in *Sam68*^{KO} and *Sam68/Slm1*^{DKO} mice was altered at the same level between the cortex, midbrain, and cerebellum (Figure S7C). Here, we tested the effect of soluble IL1RAP (sIL1RAP) on IL1RAP-induced presynaptic organization and PTP δ -induced postsynaptic organization. To this end, we employed a co-culture system wherein primary cerebellar neurons are combined with non-neuronal cells expressing a single synaptogenic molecule (Scheiffele et al., 2000) (Figures 5B and S7D). Cerebellar culture is a highly homogeneous neuron culture, which is appropriate for this assay. IL1RAP-hemagglutinin (HA)-expressing HEK293T cells triggered robust levels of presynaptic differentiation, as measured by recruitment of the presynaptic marker synaptobrevin (VAMP2) (Figure S7E left). By contrast, co-expression with sIL1RAP-HA in HEK293T cells or introduction of sIL1RAP-HA into the cultured neurons with lentivirus significantly reduced the recruitment of the presynaptic marker, demonstrating the competitive effect of sIL1RAP on synapse organization mediated by IL1RAP-PTP δ interaction. The paralog IL1RAP-L1-expressing HEK293T cells also triggered presynaptic differentiation (Figure S7E middle). Similar to IL1RAP, co-expression with sIL1RAP-HA in HEK293T cells significantly reduced IL1RAP-L1-induced recruitment of the presynaptic marker (Figure S7E middle) but did not affect neuroligin-1-induced recruitment (Figure S7E right), confirming the competitive effect of sIL1RAP on other PTP δ -mediated synapse organization. We next examined the influence of sIL1RAP on postsynaptic recruitment onto PTP δ -expressing

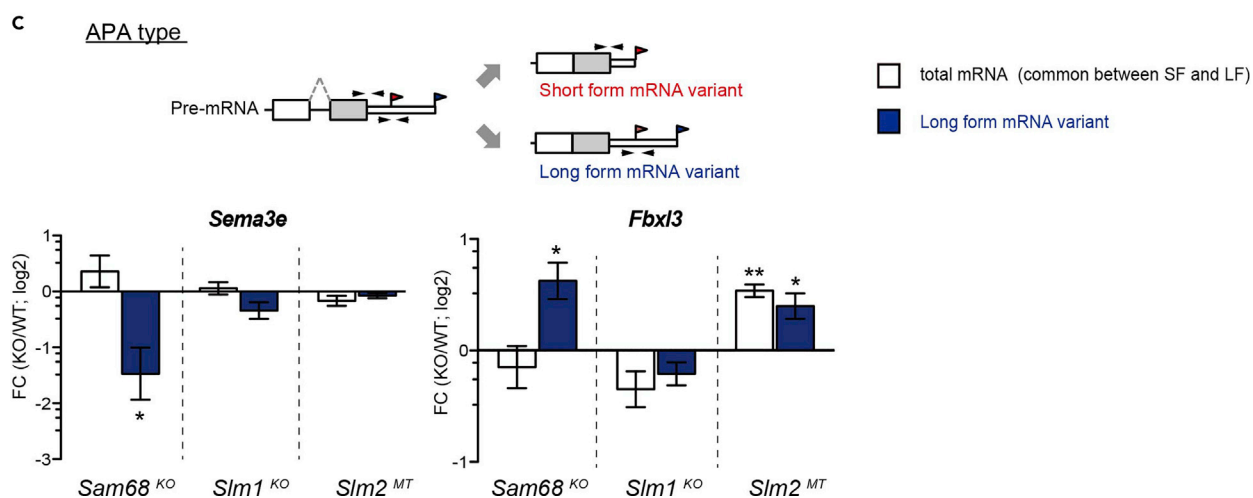
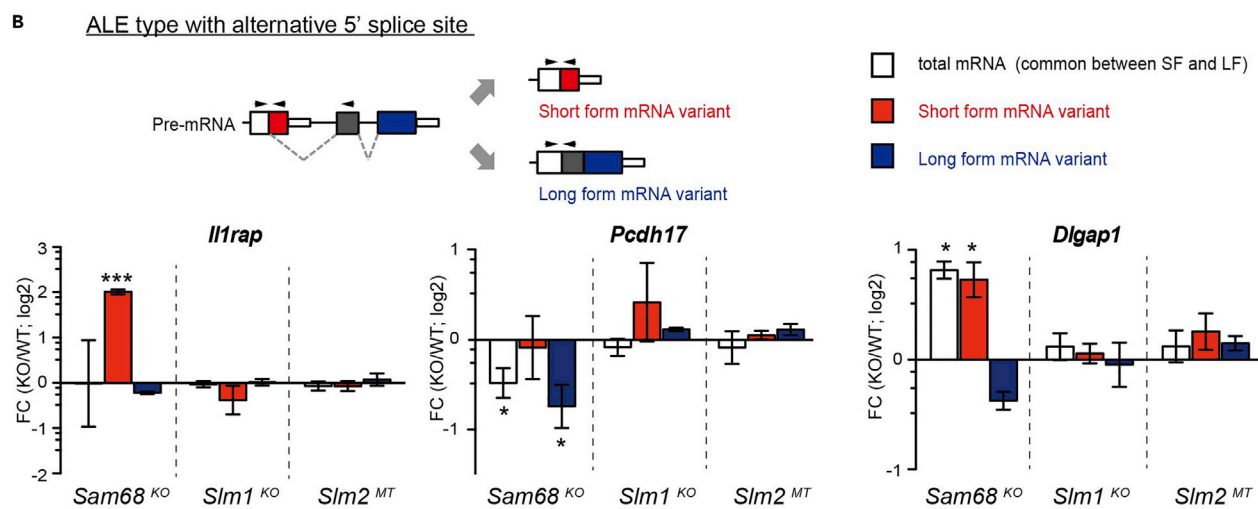
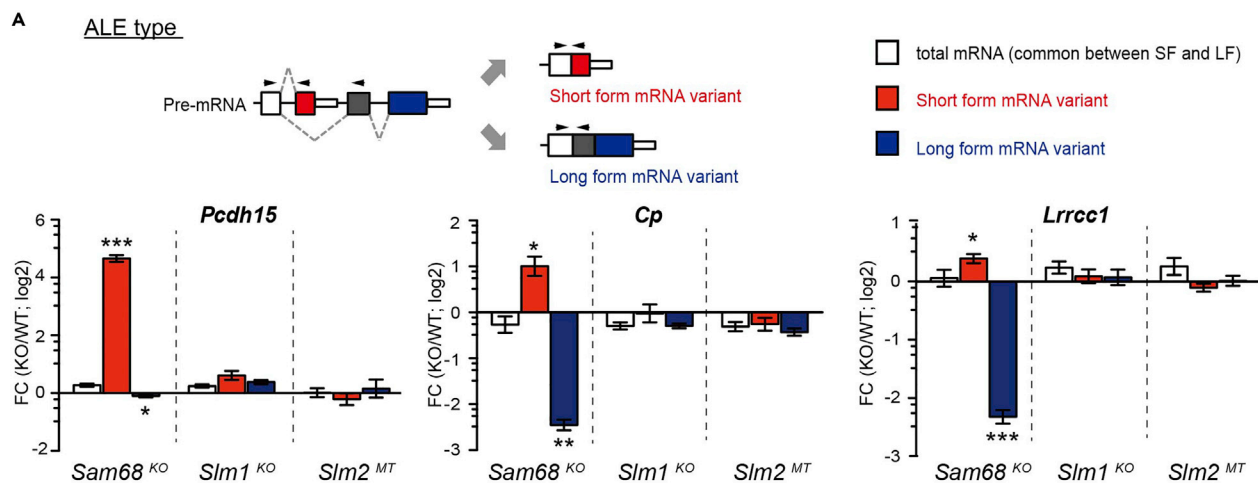


Figure 3. SAM68-Specific Splicing of Alternative 3' UTR Exons in the Nervous System

The usage of alternative last exon (ALE) or alternative polyadenylation (APA) of candidate RNA substrates was validated by RT-qPCR analysis using adult midbrains from WT, *Sam68*^{KO}, *Slm1*^{KO}, and *Slm2*^{MT} mice. Fold change (FC) and significant differences were compared with WT mice. The threshold cycle (CT) value of total transcripts was normalized to that of *Gapdh*, whereas the relative quantification (RQ) value of each alternative isoform was normalized to that of each total mRNA (n = 3–6 animals per genotype).

(A) ALE: Three genes, *Cp* (Ceruloplasmin), *Pcdh15* (Protocadherin 15), and *Lrrcc1* (leucine-rich repeat and coiled-coil domain-containing protein 1).

(B) ALE with alternative 5' splice sites: Three genes, *Dlgap1* (disk large-associated protein 1), *Il1rap* (interleukin-1 receptor accessory protein), and *Pcdh17* (protocadherin 17).

(C) Alternative polyadenylation type (APA): Two genes, *Fbxl3* (F-box/LRR-repeat protein3) and *Sema3e* (semaphorin 3e). Data are presented as the mean ± SEM. Significance is indicated as follows: ***p < 0.001; **p < 0.01; *p < 0.05; Student's t test.

HEK293T cells when sIL1RAP is co-expressed. Co-culture assay showed that PTPδ-expressing HEK293T cells induced postsynaptic differentiation, as measured by recruitment of the postsynaptic marker PSD95 (Figure 5C). Co-expression with sIL1RAP-HA in HEK293T cells also significantly affected PTPδ-induced recruitment of the postsynaptic marker, but did not influence NRX1β-induced recruitment. Synaptogenic activity was severely reduced when co-cultured with *Il1rap* knockdown cerebellar neurons (Figure S7F), confirming that PTPδ-induced post-synaptogenic activity of cerebellar neurons might be largely dependent on transsynaptic interaction with IL1RAP rather than the other partner (e.g., IL1RAP-L1) in cerebellar neurons. We then tested PTPδ-induced synaptogenic activity on a co-culture system combined with *Sam68*^{KO} neurons. We found that PTPδ-induced postsynaptic assembly in *Sam68*^{KO} neurons was significantly lower than in WT neurons, whereas NRX1β-induced assembly was comparable between WT and *Sam68*^{KO} neurons (Figure 5D). Therefore, these results suggest that proper ALE selection of *Il1rap* by SAM68 is required for synaptogenic signaling through transsynaptic IL1RAcP/IL1RAP-L1-PTPδ interaction.

Soluble IL1RAP Disturbs IL-1-Induced Ca²⁺ Influx Mediated through NMDAR Activation

Reportedly, interleukin (IL)-1 mediates not only inflammatory activity in pathological conditions but also long-term potentiation and memory formation in physiological situations by interaction with the IL-1 receptor (IL1R1) (Yirmiya et al., 2002). Such effects of IL-1 are mediated by IL1RAP. IL1RAP governs IL-1β-mediated N-methyl-D-aspartic acid (NMDA) receptor (NMDAR) activation through NR2A phosphorylation by Src family kinases in the hippocampal neurons (Figure 5A) (Huang et al., 2011). Actually, we confirmed that IL-1 and IL-1R1 transcripts were expressed in cortical and hippocampal regions (Figures S7A and S7B). Therefore, to test whether aberrant usage of *Il1rap* ALE could influence NMDAR-dependent plasticity, we examined the effect of sIL1RAP on NMDAR-dependent Ca²⁺ influx mediated through IL-1 signaling in the cultured hippocampal neurons. As NMDA (20 μM)-induced Ca²⁺ influx is potentiated at a low concentration of IL-1β (0.01 ng/mL) (Huang et al., 2011), we performed intracellular Ca²⁺ imaging using Fluo-4 AM in cultured hippocampal neurons under similar experimental conditions, as previously reported (Huang et al., 2011). We observed elevation of Ca²⁺ level, as measured by fluorescence of Fluo-4 in control neurons for a few minutes after NMDA application in the presence of 0.01 ng/mL of IL-1β (Figure 5E). Consistent with the previous report, Ca²⁺ elevation was significantly reduced in *Il1rap* knockdown neurons. In line with the knockdown effect, the Ca²⁺ elevation was significantly lower in sIL1RAP-HA-expressing neurons (Figure 5E). We confirmed the neuronal secretion of sIL1RAP-HA from cultured hippocampal neurons (Figure S7G). We further tested the NMDAR-dependent plasticity in *Sam68*^{KO} hippocampal neurons. Notably, Ca²⁺ elevation was significantly lower in *Sam68*^{KO} neurons, but not in *Slm1*^{KO} ones (Figure 5F). These results indicate that sIL1RAP impairs IL-1-induced Ca²⁺ influx mediated through NMDAR activation by antagonizing neuronal IL-1 signaling.

SAM68 Directly Binds to the Cryptic Polyadenylation Signal Sequence on Intron 8 of *Il1rap*

To address the molecular mechanism by which SAM68 targets the significant number of ALEs, we attempted to identify the recognition element of SAM68 for ALE splicing. Reportedly, the canonical poly(A) signal (PAS) sequences (AAUAAA) are optimal binding sites for SAM68 (Feracci et al., 2016; Ray et al., 2013). A recent study suggested that SAM68 masks this intronic PAS to prevent premature termination of the transcript through aberrant alternative polyadenylation (La Rosa et al., 2016). Therefore, to identify the cryptic PAS at the intronic sequence of *Il1rap*, we performed 3' rapid amplification of cDNA ends analysis from *Sam68*^{KO} brains and detected two major transcripts of *Il1rap* exon 8b (Figure S8A, arrows). The sequence analyses confirmed that the two transcripts were the full-length of exon 8b (exon 8b LF) and shorter ones (exon 8b SF) (Figures 6A and S8B). Actually, we found that the 3' UTR of exon 8b contains two putative PAS sites (PAS1 and PAS2) (Figure 6A, blue boxes). Here, RNA-seq showed that most of the transcript reads were terminated around PAS1 in *Sam68/Slm1*^{DKO} brains (Figure 6B). Although an RT-qPCR study detected

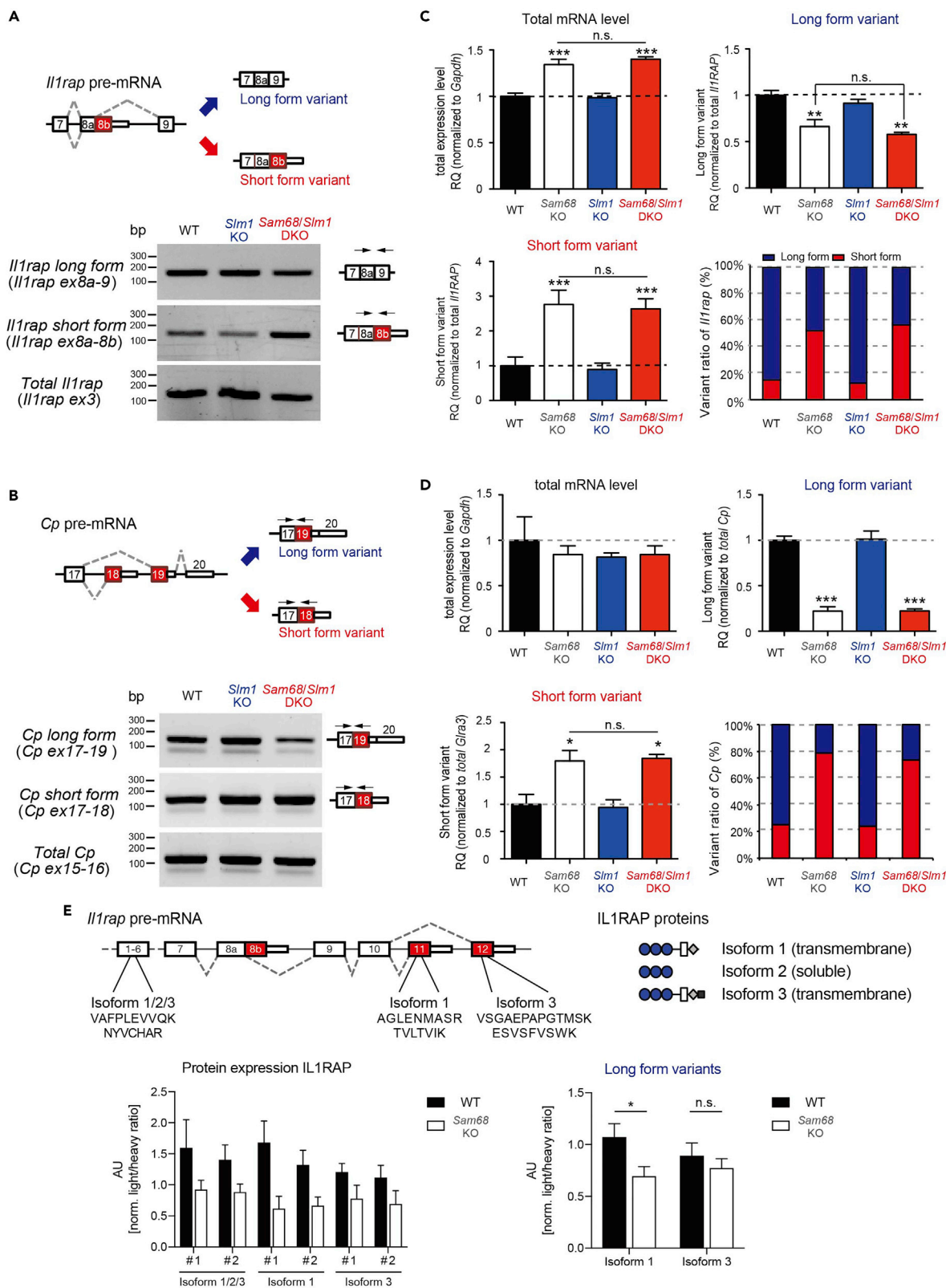


Figure 4. *Sam68*^{KO} Causes Atypical Long-to-Short Isoform Conversion of *Il1rap* and *Cp* via Aberrant Usage of ALEs

(A and B) Schematic illustration of alternative exon choice at *Il1rap* exon 8 and *Cp* at exon 13 (top panel) and the representative gel images of semi-quantitative RT-PCR with these 3' UTR exon choices in midbrains from WT, *Slm1*^{KO}, and *Sam68/Slm1*^{DKO} mice (bottom panel). (A) Exon 8b on *Il1rap* and (B) exon 13 on *Cp*.

(C and D) Relative levels of total mRNA and two alternative isoforms (LF and SF variants) and abundance ratio of SF (red) to LF (blue) between midbrains from WT, *Sam68*^{KO}, *Slm1*^{KO}, and *Sam68/Slm1*^{DKO} mice by RT-qPCR. The RQ value of total transcripts was normalized to that of *Gapdh*, whereas the RQ value of each alternative isoform was normalized to that of the total transcripts. For the abundance ratio of SF to LF, the percentage of the SF variant was largely estimated from the CT value (CT^{SF}) directly compared with that of LF (CT^{LF}) at the same threshold set for the CT value. RQ^{LF} + RQ^{SF} values for the total transcript level were set to 100%. RQ value of two transcripts was normalized to that of *Gapdh*; (C) *Il1rap* (D) *Cp* (n = 3–6 animals per genotype).

(E) Quantification of IL1RAP protein isoforms by parallel reaction monitoring (PRM). To quantify low-abundant protein isoforms, heavy reference peptides for Isoform 1/2/3 (total), Isoform 1, and Isoform 3 of IL1RAP were used in PRM-liquid chromatography-mass spectrometry. Plots show normalized endogenous (light) to reference (heavy) peak intensities of WT and *Sam68*^{KO} hippocampal samples (n = 5 per genotype) or average changes between genotypes for Isoform 1 and 3 (Isoform 1/2/3 [total] set as reference). Data are presented as the mean ± SEM. Significance is indicated as follows: ***p < 0.001; **p < 0.01; *p < 0.05. One-way ANOVA followed by Bonferroni's test.

the transcripts of exon 8b LF in *Sam68*^{KO} brains by using LF-unique primer set (primer 3) when compared with those of WT, it appeared that the amount was very small (only 2-fold higher compared with that of WT) (Figure S8C). These data indicate that the major transcripts in *Sam68*^{KO} brains are exon 8b SF. Indeed, the sequences of PAS1 were completely conserved between humans and mice (Figure S8D). Therefore PAS1 is possibly the most actionable in the absence of SAM68.

Expectedly, UV cross-linked RNA immunoprecipitation with SAM68 antibody in WT brains showed the assembly of SAM68 near PAS1, whereas binding in other regions was much weaker (Figures 6C and 6D). To further test the direct binding to PAS1, we examined the binding of SAM68 to synthetic RNA oligonucleotides spanning 30 bases of the PAS1 region (Figure 6E). The *Il1rap* 8b UTR WT probe (PAS1 WT) yielded efficient binding of endogenous SAM68 from brain extracts in the pull-down assays (Figure 6F). Furthermore, mutation of two nucleotides in a presumptive SAM68-binding PAS site (PAS1 a/c mut) significantly reduced the recovery of SAM68 (Figures 6E and 6F), demonstrating that endogenous SAM68 can directly recognize the PAS1 sequence. Under the same conditions, the other RBP, Rbfox1, was not recovered in the precipitates. Therefore, these data suggest that SAM68 regulates ALE selection through direct binding to the cryptic PAS in intron 8 of WT brains.

Tissue-Specific SAM68 Expression Determines ALE Selection in Spatial Fashion

Given that a significant number of SAM68-targeted transcripts could be expressed in tissues other than the brain, it would be of interest to explore how SAM68-dependent ALE selection is controlled in those other tissues. Therefore, we examined the expression profiles of *Il1rap*, *Cp*, *Pcdh15*, and *Lrrcc1* in various tissues. We observed that transcripts of *Il1rap*, *Cp*, and *Lrrcc1* were detected ubiquitously (Figure S9A). On the other hand, expression of SAM68 exhibited a tissue-specific pattern (Figure S9B). In particular, SAM68 expression appears to be very subtle in the liver. RT-qPCR also showed low expression of not only *Sam68* but also *Slm1* in the liver at the transcript level (Figure S9C). We then examined the ratio of *Il1rap* and *Cp* splicing isoforms (LF versus SF) in several tissues. The ratio was highly variable among tissues (Figure 7A). In contrast to the brain, both major transcripts were the SF variant in the liver, in which SAM68 expression is very low. Indeed, we found that the amount of SAM68 is inversely correlated with the abundance of the SF variant (*Il1rap*, R² = 0.85, p = 0.008; *Cp*, R² = 0.86, p = 0.04, Figure 7B). We also observed that the amount of the *Il1rap* SF variant was significantly increased in the *Sam68*^{KO} lung and brain compared with the WTs (Figure 7C), whereas ectopic expression of SAM68 in primary liver cell culture significantly reduced the SF variant (Figure 7D). These results showed that ALE selection of these SAM68 targets is highly dependent on the expression dose of SAM68.

Furthermore, we observed that although SAM68 is not expressed in the normal mouse liver, it was strongly expressed in a human hepatocarcinoma cell line, i.e., HepG2 cells (Figure 7E). In association with the strong expression of SAM68, we found that the ratio of the *Il1rap* SF variant in HepG2 cells was markedly lower (<40%), compared with that in the normal mouse liver (Figure 7F). To verify whether the low amount of the *Il1rap* SF variant in HepG2 cells is due to the aberrant expression of SAM68 in carcinoma cells, we examined the knockdown effect of human SAM68 (hSAM68) on the ratio of *Il1rap* splicing variants in HepG2 cells. We found that knockdown of hSAM68 partially, but significantly, increased the *Il1rap* SF variant (Figure 7G). These results further suggest that SAM68 is a dominant regulator for ALE selection of *Il1rap* throughout the whole tissue. Thus, the absence of SAM68 causes a long-to-short isoform switch of the neuronal targets in non-neuronal tissues (Figure 7H),

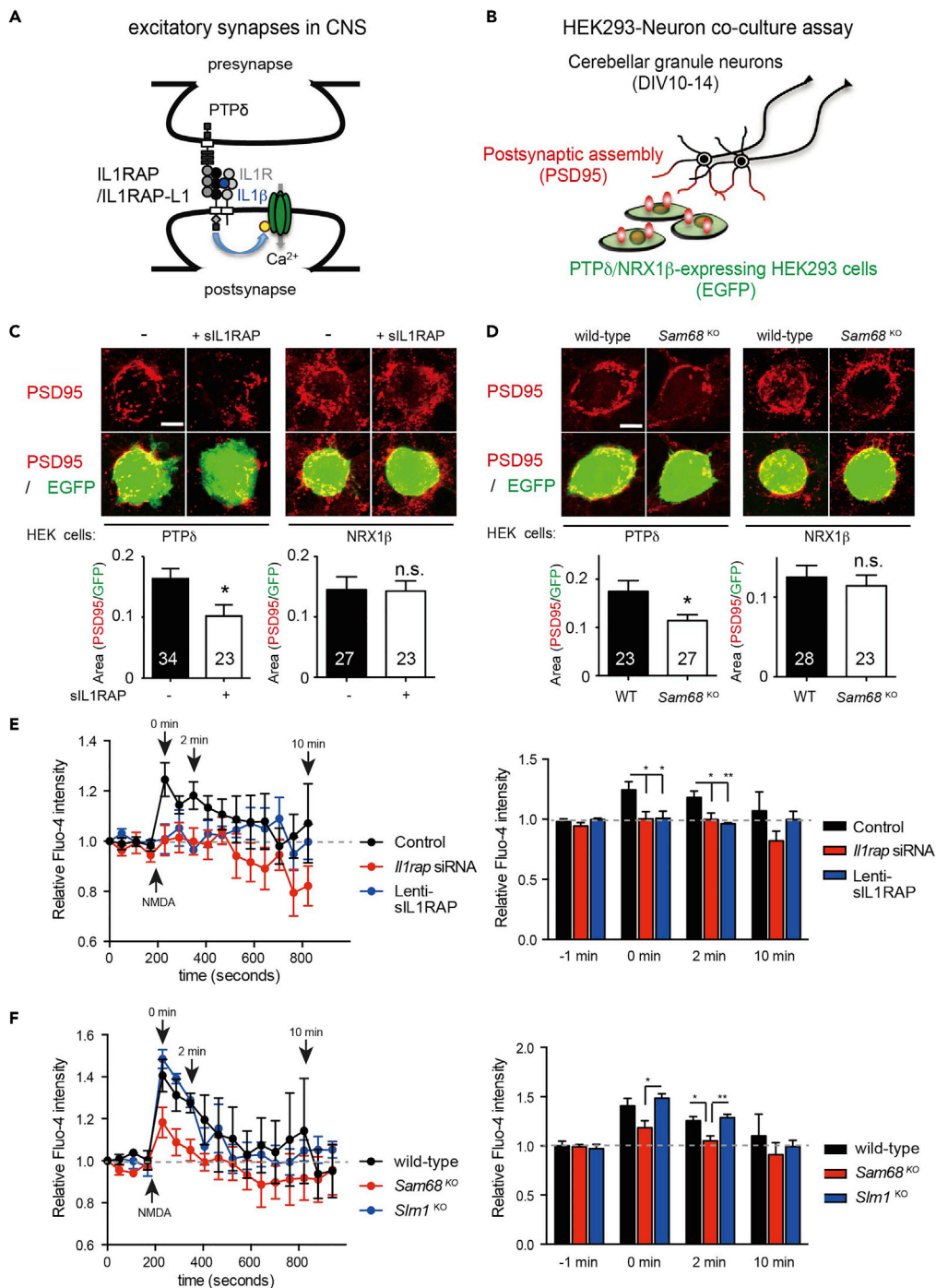


Figure 5. Soluble IL1RAcP Disturbs PTPδ-Induced Synaptogenic Signaling and IL-1-Mediated NMDAR Function in the Nervous System

(A) Illustration of excitatory synapse organization through synaptic interaction of IL1RAP and the related-protein IL1RAP-L1 with PTPδ, and IL-1-induced potentiation of NMDAR-mediated calcium influx through interaction with IL-1 receptor (IL1R) in the CNS.

(B) Schematic illustration of neuron-HEK293T cell co-culture assay. To examine IL1RAP-mediated postsynaptic assembly, HEK293T cells expressing PTPδ or neuexin-1β (NRX1β)-HA were co-cultured with cerebellar neurons (DIV10-14).

(C and D) Soluble IL1RAP (sIL1RAP) disturbs PTPδ-induced synaptogenic signaling. Postsynaptic assembly on HEK293T cells was detected by immunostaining with postsynaptic marker, PSD-95. (C) HEK293T cells expressing PTPδ or NRX1β-HA with or without sIL1RAP-HA (ratio 1:1). (D) HEK293T cells expressing PTPδ or NRX1β were co-cultured with

Figure 5. Continued

cerebellar granule neurons from WT or *Sam68*^{KO} cerebella (n = 23–34 cells/each group in >10 separated fields [see the number on each graph column]) Scale bar, 5 μ m.

(E and F) Calcium imaging with Fluo-4 AM in cultured hippocampal neurons. Soluble IL1RAP disturbs IL-1-induced potentiation of calcium influx mediated via NMDARs. Intracellular calcium levels were measured by Fluo-4 intensity. Quantification of intracellular calcium level at 1 min before NMDA stimulation (Pre) and at 0, 2, and 10 min after stimulation. (E) The traces (left) and quantification (right) of the relative intracellular calcium level in control neurons, *Il1rap* knockdown neurons, and sIL1RAP-HA-expressing neurons with lentiviral infection (control, n = 130 fields; *Il1rap* knockdown, n = 50 fields; sIL1RAP-HA expressing, n = 30 fields, in three independent experiments). (F) The traces (left) and quantification (right) of the relative intracellular calcium level in wild-type, *Sam68*^{KO}, and *Slm1*^{KO} neurons (wild-type, n = 50 fields; *Sam68*^{KO}, n = 50 fields; *Slm1*^{KO} expressing, n = 40 fields, in three independent experiments). Data are presented as the mean \pm SEM. Significance is indicated as follows: **p < 0.01; *p < 0.05. Student's t test in (C and D); one-way ANOVA followed by Dunnett's test in (E and F).

indicating that the SAM68 expression level is critical for the tissue-specific selection of alternative 3' UTR isoforms through ALE choice. Indeed, whereas atypical sIL1RAP could impair PTP δ -mediated synapse organization in the nervous system (Figure 5), physiological sIL1RAP in plasma plays a homeostatic role in IL-1 signaling by antagonizing the interaction with IL-1R1 in the immune system (Jensen et al., 2000; Smeets et al., 2005). Therefore, SAM68-dependent ALE selection could be necessary to exert distinct functions of ubiquitously expressed molecules between the nervous and the non-nervous systems (Figure 7).

DISCUSSION**Distinct Alternative Splicing Activity between SAM68 and the Related Proteins SLMs**

We showed that neuronal alternative splicing by STAR family proteins is an important mechanism for functional diversification. Here, we conducted transcriptomic analyses using *Slm1*^{KO} and *Sam68/Slm1*^{DKO} brains and showed a different splicing activity between SAM68 and SLM1. This study focused on the neuronal isoform selection in 3' UTR by SAM68 and demonstrated their functional aspects through the identification of a novel target IL1RAP in neurons (Figure 5). Very recently, two articles also elucidated the interaction between SAM68 and U1 small nuclear ribonucleoprotein particle (snRNP) as a global mechanism underlying ALE regulation by SAM68 (Naro et al., 2019; Subramania et al., 2019), supporting our findings in the CNS. U1 snRNP prevents premature transcript termination by inhibition of cryptic PASs (Berg et al., 2012; Kaida et al., 2010). Therefore, our findings on ALE selection in CNS also might be largely explained by the interaction with U1 snRNP. However, given that the U1 binding-like sequences were not observed around cryptic PAS1 on *Il1rap* (see Figure S8), additional mechanism also could be possible. Considering the direct binding to cryptic PAS in WT brains (Figure 6), another possibility is that SAM68 may block the recruitment of such 3' end machineries on the PAS as the CPSF and CstF to prevent the proximal termination of *Il1rap* pre-mRNA. ALE selection is related to alternative polyadenylation; such 3' end formation factors have been shown to play a role in alternative splicing (Misra and Green, 2016).

In addition to the difference in splicing activities between SAM68 and SLM1, this study also suggested a difference between SLM1 and another family protein, SLM2. We newly mapped the entire SLM1-dependent program and revealed that a significant number of exons seemed to be altered in *Slm1*^{KO} brains (Figure 1 and Table S2), whereas SLM2 encodes a highly selective alternative splicing program that regulates only a few synaptic molecules (Traunmuller et al., 2016). Regardless of the high structural homology between SLM1 and SLM2 (Di Fruscio et al., 1999), the large functional difference between the two closely related proteins is very surprising. We previously showed that SAM68 can heteromerize with SLM1, but not with SLM2 (Iijima et al., 2014), which suggests that endogenous SLM2 ordinarily exists as a homodimer. Thus dimer formation is intrinsically different between SLM1 and SLM2. Increased RNA affinity through dimer formation is a critical parameter enabling SLM proteins to select their functional targets with the transcriptome (Feracci et al., 2016). Therefore, one possibility is that the structural difference in dimer interface between SLM1 and SLM2 complexes results in distinct splicing programs. However, numerous questions on the functional difference between STARS remains to be addressed in future studies.

Critical Role of Proper ALE Selection of *Il1rap* between the Nervous and Other Systems by Distinct SAM68 Expression Level

This study revealed that SAM68 is a dominant factor for ALE selection of *Il1rap* in the nervous system. mL1RAP is necessary for organizing excitatory synapses through transsynaptic interaction with PTP δ in

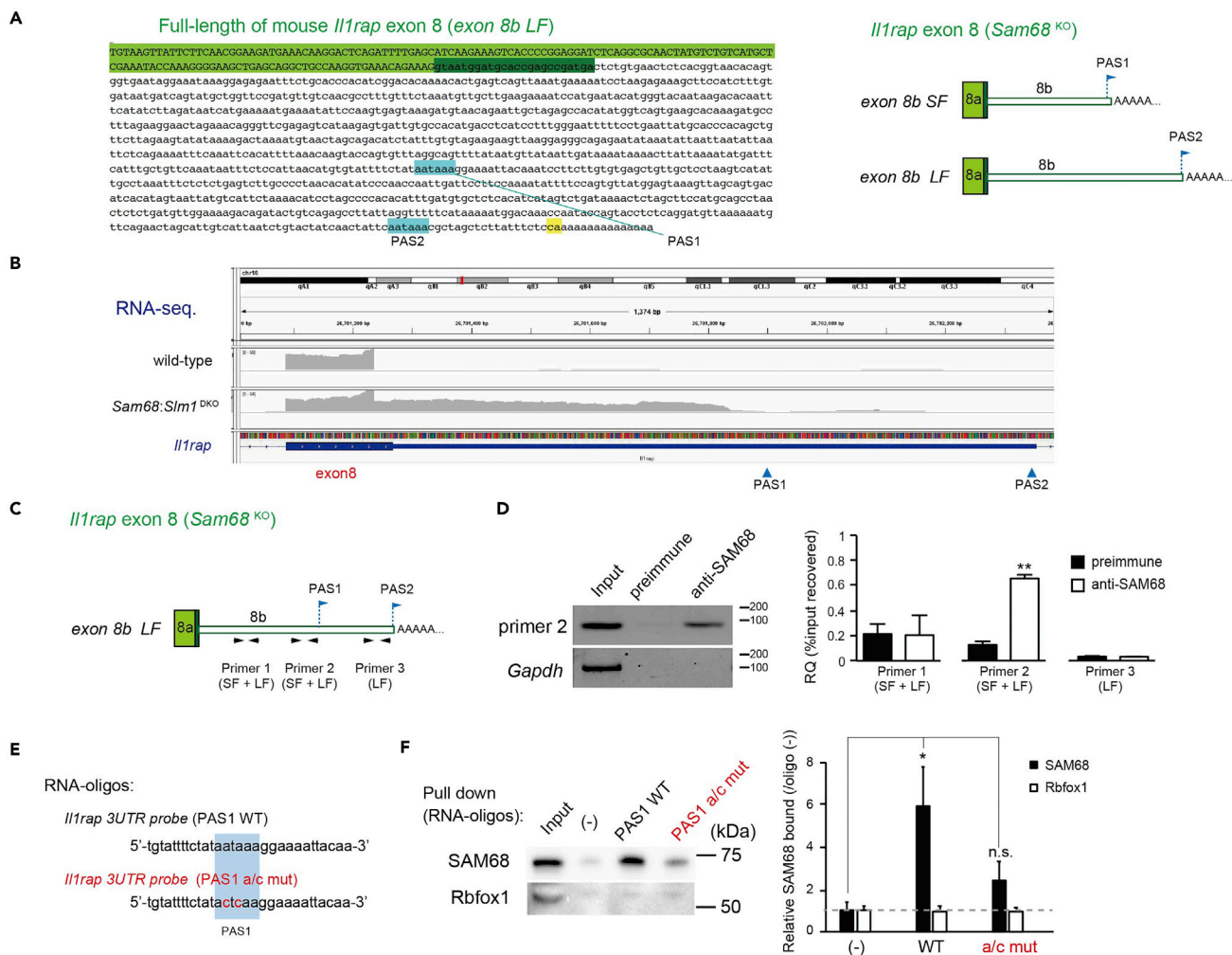


Figure 6. SAM68 Directly Binds to Cryptic PAS in the Intron 8 of *Il1rap*

(A) The full-length cDNA sequence of *Il1rap* exon 8 (left), and the schematic illustration of the two major transcripts in *Sam68*^{KO} brains (exon 8b SF and exon 8b LF) (right). Green indicates the coding exon region, blue shows putative PAS sites on the 3' UTR.

(B) RNA-seq on *Il1rap* exon 8b in wild-type and *Sam68/Slm1*^{DKO} brains. Arrowheads represent two putative PAS sites (PAS1 and PAS2).

(C–F) Mapping of SAM68 recognition elements in *Il1rap*. (C and D) UV cross-linked RNA immunoprecipitation (CLIP) assay. (C) Positions of three primer sets used for the assay. (D) The representative gel loading images of the CLIP assay using anti-SAM68 antibody and the quantification by RT-qPCR analysis (n = 3 brains).

(E and F) Biotinylated RNA pull-down experiments. (E) Biotinylated RNA oligonucleotide probes covering the 3' UTR sequence of *Il1rap* exon 8b used in pull-down experiments. The PAS a/c mut probe contains two nucleotide changes (red). (F) The pull-down experiments with mouse adult brain extracts. Bound proteins were detected by western blot analysis with anti-SAM68 and anti-Rbfox1 antibodies. SAM68 binding was quantified by densitometric scanning of western blot signals (n = 5).

Data are presented as the mean ± SEM. Significance is indicated as follows: ***p < 0.001; **p < 0.01; *p < 0.05. Student's t test.

the CNS (Yoshida et al., 2012). This study demonstrated that, in addition to the significant reduction in mIL1RAP (Figure 4), the competitive effect of sIL1RAP could accelerate the impairment in PTPδ-mediated synapse organization (Figures 5A–5D). Reasonably, the competitive effect is supported by the X-ray structural analysis showing that the Ig domains of IL1RAP and PTPδ are the elements responsible for the heterophilic interaction (Yamagata et al., 2015). Both IL1RAP and PTPδ have several transsynaptic binding partners. PTPδ organizes synapses through interaction with IL1RAP-L1 and Slitrk3 (Takahashi et al., 2012; Yoshida et al., 2011). In addition to IL1RAP, because we demonstrated the competitive effect of sIL1RAP on presynapse assembly onto HEK293T cells expressing another paralog, IL1RAP-L1, on co-culture assays (Figure S7E), sIL1RAP may influence several related transsynaptic types of synaptogenic signaling in the CNS. We also revealed that sIL1RAP significantly affects IL-1β-induced NMDAR activation in hippocampal neurons (Figures 5E and 5F). Thus, this study suggests that proper

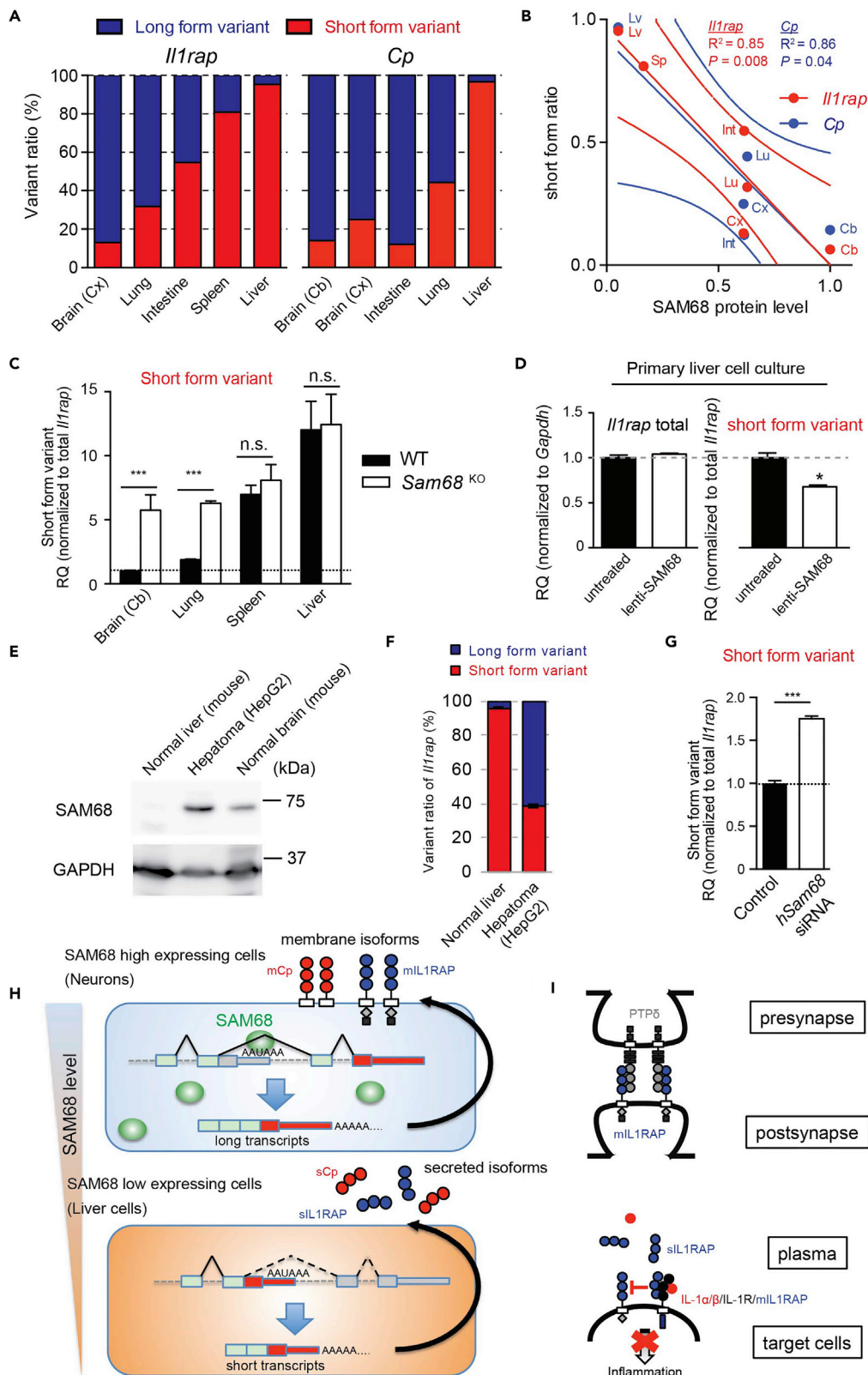


Figure 7. The Distinct Amount of SAM68 Is Responsible for Proper 3' UTR Isoform Selection of *Il1rap* and *Cp* in the Nervous and Non-nervous Systems

(A) Abundance ratio of SF to LF in the brain, lung, intestine, spleen, and liver of WT mice. For the abundance ratio of SF to LF, the percentage of the SF variant was largely estimated from the CT value (C_T^{SF}) directly compared with that of LF (C_T^{LF}) at the same threshold set for the CT value. $RQ^{LF} + RQ^{SF}$ values for total *Il1rap* were set to 100%. RQ value of two transcripts was normalized to that of *Gapdh* ($n = 3-4$ animals per group).

(B) Reciprocal correlation between SAM68 level and production of *Il1rap* and *Cp* SFs. SAM68 was quantified by western blot analysis. The value for the cerebellum was set to 1.0. Correlation coefficients between SAM68 and the SF transcript of *Il1rap* and *Cp* (right) were determined in the scatterplot analysis. The gray lines in the scatterplot are the 95% confidence limit of the best fit line.

(C) Quantification of the SF variant of *Il1rap* between brain and non-neuronal tissues (lung, intestine, liver, and spleen) from WT and *Sam68*^{KO} mice by RT-qPCR. The RQ value of total transcripts was normalized to that of total *Il1rap* ($n = 3$ animals per genotype). RQ values for wild-type brain (Cb) were set to 1.0.

(D) Quantification of the SF variant of *Il1rap* between the primary liver cell cultures and the ones in which SAM68 was ectopically expressed with lentiviral infection. The RQ value of total transcripts was normalized to that of *Gapdh*. The RQ value of SF transcripts was normalized to that of total *Il1rap* ($n = 3$ cultures per group).

(E) Representative images of western blot analysis with the α -SAM68 antibody. Human hepatoma cell line, HepG2, cells aberrantly express SAM68 at high level.

(F) Low production of the *Il1rap* SF variant in HepG2 cells. The abundance ratio of SF to LF was compared between the normal mouse liver and HepG2 cells ($n = 3-4$ cultures per group).

(G) Restoration of aberrant ALE selection in HepG2 cells by knockdown of SAM68. Knockdown of aberrantly expressing SAM68 partially but significantly increased the level of the *Il1rap* SF isoform in HepG2 cells. The RQ value of SF transcripts was normalized to that of total *Il1rap* ($n = 3-4$ cultures per group).

(H and I) Model of tissue-specific isoform selection of *Il1rap* and *Cp* through usage of ALEs between the brain and liver by physiologically expressed SAM68. (H) The neurons strongly express SAM68, so that they dominantly produces the membrane forms. In contrast to the brain, secreted forms lacking transmembrane domain or glycosylphosphatidylinositol anchor are abundantly produced in the liver. (I) SAM68-specific ALE selection is required for the organization of IL1RAP-dependent excitatory synapses through transsynaptic interaction with PTP δ in the nervous system. On the other hand, absence of SAM68 causes the release of IL1RAP into the plasma, which could be necessary for homeostatic control of IL1-mediated inflammation.

Data are presented as the mean \pm SEM. Significance is indicated as follows: *** $p < 0.001$; * $p < 0.05$; Student's t test.

ALE usage by SAM68-specific splicing is critical for both aspects of synaptic organization and plasticity in the CNS.

In contrast to the brain, the liver is thought to be a major source of sIL1RAP, which is suggested to play an important role in the homeostasis of IL-1 signaling by antagonizing the interaction of IL1RAP with IL-1R1 in the immune system (Jensen et al., 2000; Smeets et al., 2005). The reduced level of physiological sIL1RAP in the plasma is in fact implicated in several diseases (Bozaoglu et al., 2014; Michaud et al., 2014). Thus, tissue-specific SAM68 expression could play a critical role in distinct functions of ubiquitously expressed proteins between the nervous and non-nervous systems through ALE selection (Figures 7H and 7I).

Regulatory Functions of the SAM68 Splicing Program Dedicated to Alternative 3' UTR Isoform Diversity

Thousands of mammalian genes encode alternatively spliced isoforms in their 3' UTR (Miura et al., 2013; Tian et al., 2005). Here, we demonstrated that SAM68 is required for the spatial control of alternative 3' UTR isoforms between the nervous and the other systems by identification of new SAM68 targets (Figure 7). Importantly, GO analyses implied that SAM68 targets the 3' UTR exons of multiple transcripts that encode neuronal membrane or secreted proteins (Figures 1E and 2D). The biochemical studies indeed found drastic shift to short isoforms by aberrant ALE selection in *Sam68*^{KO} brains, which could result in membrane-to-secreted isoform conversion at the protein level. Thus the findings strongly suggest that SAM68 is a key regulator for shaping the diversity of neuronal 3' UTR isoforms in the nervous system.

The other intriguing point regarding alternative 3' UTR selection is the molecular control at the transcript level. This study also found that SAM68 regulates not only ALE but also APA (Figures 2 and 3C), which alters the length of the 3' UTR itself. Such alternative 3' UTR diversity by APA and ALE contributes to the posttranscriptional processes such as translation, mRNA stability, and subcellular localization during development (Di Giammartino et al., 2011; Taliaferro et al., 2016) and dendritic localization and the local translation in the

nervous system (Tushev et al., 2018). Therefore, it would be of interest to explore how the ALE/APA-mediated mechanism by SAM68 contributes to molecular functions at the transcript level in a future study. Overall, although the mechanism by which a specific subset of 3' UTR exons is controlled by SAM68-specific splicing should be examined, our findings could provide a general principle underlying the control of alternatively spliced 3' UTR isoforms.

Limitations of Study

In this study, we performed transcriptomic analysis using SAM68 knockout and SAM68/SLM1 double-knockout midbrains and revealed a different alternative splicing activity between SAM68 and SLM1; we characterized alternative 3' UTR selection by SAM68-specific splicing in the nervous system. However, the open questions on the mechanism underlying the differential splicing activity between SAM68 and the related family proteins remains to be addressed in future studies.

Our findings extend the understanding on the neuronal function of SAM68, in particular through the identification of IL1RAP as a new SAM68 target. However, the physiological consequences were mainly obtained by neuronal culture system. Further studies are needed to confirm the functional relevance *in vivo*.

METHODS

All methods can be found in the accompanying [Transparent Methods supplemental file](#).

DATA AND CODE AVAILABILITY

The data presented in this article have been deposited in NCBI's Gene Expression Omnibus and are accessible through GEO Series accession number GSE110258.

SUPPLEMENTAL INFORMATION

Supplemental Information can be found online at <https://doi.org/10.1016/j.isci.2019.11.028>.

ACKNOWLEDGMENTS

We are grateful to Dr. Yoshida (Toyama University) for kindly providing materials and reading the manuscript; to Drs. Sumiyoshi (Tokai University), Kamiya (Tokai University), and Müller (Scripps Res. Inst., USA) for kindly providing materials; to Dr. Yano (Niigata University) for reading the manuscript and providing constructive comments; to Drs. Hidaka (Kouchi University) and Umakawa for experimental support; and to Dr. Schmidt and the Proteomics Core Facility (Basel University) for conducting proteomic analysis. We also thank all the members of the Support Center for Medical Research and Education at Tokai University for experimental support and maintenance of experimental animals. This work was supported by JSPS KAKENHI (grants 15H04277 and 15K14355), the Mitsubishi Foundation (Mitsubishi Zaidan), the Yamada Science Foundation, the Takeda Science Foundation, the Naito Foundation, and Mochida Memorial Foundation for Medical and Pharmacological Research (all to T.I.). The work in the Scheiffele lab was supported by ERC Advanced Grant SPLICECODE and funds from the Swiss National Science Foundation.

AUTHOR CONTRIBUTIONS

Y.I., Masami Tanaka, and T.I. conceived and designed the experiments; Y.I., Masami Tanaka, S.S., D.H., Y.S., N.A., C.O., T.I., and M.I. performed the experiments; Y.I., Masami Tanaka, S.S. D.H., Masayuki Tanaka, C.O., and T.I. analyzed the data; S.S., C.O., M.T., Y.I., M.O., P.S., and T.I. contributed reagents/materials/analysis tools; Y.I., Masami Tanaka, S.S., and T.I. wrote the paper.

DECLARATION OF INTERESTS

The authors declare no competing interests.

Received: April 5, 2019

Revised: July 9, 2019

Accepted: November 13, 2019

Published: December 20, 2019

REFERENCES

- Aoto, J., Martinelli, D.C., Malenka, R.C., Tabuchi, K., and Sudhof, T.C. (2013). Presynaptic neuexin-3 alternative splicing trans-synaptically controls postsynaptic AMPA receptor trafficking. *Cell* 154, 75–88.
- Barbosa-Morais, N.L., Irimia, M., Pan, Q., Xiong, H.Y., Guerousov, S., Lee, L.J., Slobodenic, V., Kutter, C., Watt, S., Colak, R., et al. (2012). The evolutionary landscape of alternative splicing in vertebrate species. *Science* 338, 1587–1593.
- Baudouin, S., and Scheiffele, P. (2010). SnapShot: neuroligin-neurexin complexes. *Cell* 141, 908, 908.e1.
- Berg, M.G., Singh, L.N., Younis, I., Liu, Q., Pinto, A.M., Kaida, D., Zhang, Z., Cho, S., Sherrill-Mix, S., Wan, L., et al. (2012). U1 snRNP determines mRNA length and regulates isoform expression. *Cell* 150, 53–64.
- Boucard, A.A., Chubykin, A.A., Comoletti, D., Taylor, P., and Sudhof, T.C. (2005). A splice code for trans-synaptic cell adhesion mediated by binding of neuroligin 1 to alpha- and beta-neurexins. *Neuron* 48, 229–236.
- Bozaoglu, K., Attard, C., Kulkarni, H., Cummings, N., Diego, V.P., Carless, M.A., Shields, K.A., Johnson, M.P., Kowlessur, S., Dyer, T.D., et al. (2014). Plasma levels of soluble interleukin 1 receptor accessory protein are reduced in obesity. *J. Clin. Endocrinol. Metab.* 99, 3435–3443.
- Chawla, G., Lin, C.H., Han, A., Shiu, L., Ares, M., Jr., and Black, D.L. (2009). Sam68 regulates a set of alternatively spliced exons during neurogenesis. *Mol. Cell. Biol.* 29, 201–213.
- Di Fruscio, M., Chen, T., and Richard, S. (1999). Characterization of Sam68-like mammalian proteins SLM-1 and SLM-2: SLM-1 is a Src substrate during mitosis. *Proc. Natl. Acad. Sci. U S A* 96, 2710–2715.
- Di Giammartino, D.C., Nishida, K., and Manley, J.L. (2011). Mechanisms and consequences of alternative polyadenylation. *Mol. Cell* 43, 853–866.
- Ehrmann, I., Dalgliesh, C., Liu, Y., Danilenko, M., Crosier, M., Overman, L., Arthur, H.M., Lindsay, S., Clowry, G.J., Venables, J.P., et al. (2013). The tissue-specific RNA binding protein T-STAR controls regional splicing patterns of neuexin pre-mRNAs in the brain. *PLoS Genet.* 9, e1003474.
- Ehrmann, I., Gazzara, M.R., Pagliarini, V., Dalgliesh, C., Kheirollahi-Chadegani, M., Xu, Y., Cesari, E., Danilenko, M., MacLennan, M., Lowdon, K., et al. (2016). A SLM2 feedback pathway controls cortical network activity and mouse behavior. *Cell Rep.* 17, 3269–3280.
- Feracci, M., Foot, J.N., Grelscheid, S.N., Danilenko, M., Stehle, R., Gonchar, O., Kang, H.S., Dalgliesh, C., Meyer, N.H., Liu, Y., et al. (2016). Structural basis of RNA recognition and dimerization by the STAR proteins T-STAR and Sam68. *Nat. Commun.* 7, 10355.
- Huang, Y., Smith, D.E., Ibanez-Sandoval, O., Sims, J.E., and Friedman, W.J. (2011). Neuron-specific effects of interleukin-1beta are mediated by a novel isoform of the IL-1 receptor accessory protein. *J. Neurosci.* 31, 18048–18059.
- Huot, M.E., Vogel, G., Zabarauskas, A., Ngo, C.T., Coulombe-Huntington, J., Majewski, J., and Richard, S. (2012). The Sam68 STAR RNA-binding protein regulates mTOR alternative splicing during adipogenesis. *Mol. Cell* 46, 187–199.
- Iijima, T., Hidaka, C., and Iijima, Y. (2016). Spatio-temporal regulations and functions of neuronal alternative RNA splicing in developing and adult brains. *Neurosci. Res.* 109, 1–8.
- Iijima, T., Iijima, Y., Witte, H., and Scheiffele, P. (2014). Neuronal cell type-specific alternative splicing is regulated by the KH domain protein SLM1. *J. Cell Biol.* 204, 331–342.
- Iijima, T., Wu, K., Witte, H., Hanno-Iijima, Y., Glatter, T., Richard, S., and Scheiffele, P. (2011). SAM68 regulates neuronal activity-dependent alternative splicing of neuexin-1. *Cell* 147, 1601–1614.
- Jensen, L.E., Muzio, M., Mantovani, A., and Whitehead, A.S. (2000). IL-1 signaling cascade in liver cells and the involvement of a soluble form of the IL-1 receptor accessory protein. *J. Immunol.* 164, 5277–5286.
- Kaida, D., Berg, M.G., Younis, I., Kasim, M., Singh, L.N., Wan, L., and Dreyfuss, G. (2010). U1 snRNP protects pre-mRNAs from premature cleavage and polyadenylation. *Nature* 468, 664–668.
- Kalsotra, A., and Cooper, T.A. (2011). Functional consequences of developmentally regulated alternative splicing. *Nat. Rev. Genet.* 12, 715–729.
- Ko, J., Fuccillo, M.V., Malenka, R.C., and Sudhof, T.C. (2009). LRRTM2 functions as a neuexin ligand in promoting excitatory synapse formation. *Neuron* 64, 791–798.
- Krueger, D.D., Tuffy, L.P., Papadopoulos, T., and Brose, N. (2012). The role of neuexins and neuroligins in the formation, maturation, and function of vertebrate synapses. *Curr. Opin. Neurobiol.* 22, 412–422.
- La Rosa, P., Bielli, P., Compagnucci, C., Cesari, E., Volpe, E., Farioli Vecchioli, S., and Sette, C. (2016). Sam68 promotes self-renewal and glycolytic metabolism in mouse neural progenitor cells by modulating Aldh1a3 pre-mRNA 3'-end processing. *Elife* 5, e20750.
- Li, N., Hebert, S., Song, J., Kleinman, C.L., and Richard, S. (2017). Transcriptome profiling in preadipocytes identifies long noncoding RNAs as Sam68 targets. *Oncotarget* 8, 81994–82005.
- Li, Q., Lee, J.A., and Black, D.L. (2007). Neuronal regulation of alternative pre-mRNA splicing. *Nat. Rev. Neurosci.* 8, 819–831.
- Lukong, K.E., and Richard, S. (2008). Motor coordination defects in mice deficient for the Sam68 RNA-binding protein. *Behav. Brain Res.* 189, 357–363.
- Matsuda, K., and Yuzaki, M. (2011). Cbln family proteins promote synapse formation by regulating distinct neuexin signaling pathways in various brain regions. *Eur. J. Neurosci.* 33, 1447–1461.
- Merkin, J., Russell, C., Chen, P., and Burge, C.B. (2012). Evolutionary dynamics of gene and isoform regulation in Mammalian tissues. *Science* 338, 1593–1599.
- Michaud, N., Al-Akoum, M., and Akoum, A. (2014). Blood soluble interleukin 1 receptor accessory protein levels are consistently low throughout the menstrual cycle of women with endometriosis. *Reprod. Biol. Endocrinol.* 12, 51.
- Misra, A., and Green, M.R. (2016). From polyadenylation to splicing: dual role for mRNA 3' end formation factors. *RNA Biol.* 13, 259–264.
- Missler, M., and Sudhof, T.C. (1998). Neuexins: three genes and 1001 products. *Trends Genet.* 14, 20–26.
- Miura, P., Shenker, S., Andreu-Agullo, C., Westholm, J.O., and Lai, E.C. (2013). Widespread and extensive lengthening of 3' UTRs in the mammalian brain. *Genome Res.* 23, 812–825.
- Naro, C., Pellegrini, L., Jolly, A., Farini, D., Cesari, E., Bielli, P., de la Grange, P., and Sette, C. (2019). Functional interaction between U1snRNP and Sam68 insures proper 3' end pre-mRNA processing during germ cell differentiation. *Cell Rep.* 26, 2929–2941.e5.
- Nguyen, T.M., Schreiner, D., Xiao, L., Traunmuller, L., Bornmann, C., and Scheiffele, P. (2016). An alternative splicing switch shapes neuexin repertoires in principal neurons versus interneurons in the mouse hippocampus. *Elife* 5, <https://doi.org/10.7554/eLife.22757>.
- Raj, B., and Blencowe, B.J. (2015). Alternative splicing in the mammalian nervous system: recent insights into mechanisms and functional roles. *Neuron* 87, 14–27.
- Ray, D., Kazan, H., Cook, K.B., Weirauch, M.T., Najafabadi, H.S., Li, X., Guerousov, S., Albu, M., Zheng, H., Yang, A., et al. (2013). A compendium of RNA-binding motifs for decoding gene regulation. *Nature* 499, 172–177.
- Razanau, A., and Xie, J. (2013). Emerging mechanisms and consequences of calcium regulation of alternative splicing in neurons and endocrine cells. *Cell Mol. Life Sci.* 70, 4527–4536.
- Sanchez-Jimenez, F., and Sanchez-Margalet, V. (2013). Role of Sam68 in post-transcriptional gene regulation. *Int. J. Mol. Sci.* 14, 23402–23419.
- Scheiffele, P., Fan, J., Choih, J., Fetter, R., and Serafini, T. (2000). Neuroligin expressed in nonneuronal cells triggers presynaptic development in contacting axons. *Cell* 101, 657–669.
- Smeets, R.L., Joosten, L.A., Arntz, O.J., Bennink, M.B., Takahashi, N., Carlsen, K., Martin, M.U., van den Berg, W.B., and van de Loo, F.A. (2005). Soluble interleukin-1 receptor accessory protein ameliorates collagen-induced arthritis by a different mode of action from that of interleukin-1 receptor antagonist. *Arthritis Rheum.* 52, 2202–2211.
- Subramania, S., Gagne, L.M., Campagne, S., Fort, V., O'Sullivan, J., Mocaer, K., Feldmuller, M., Masson, J.Y., Allain, F.H.T., Hussein, S.M., et al. (2019). SAM68 interaction with U1A modulates

U1 snRNP recruitment and regulates mTor pre-mRNA splicing. *Nucleic Acids Res.* 47, 4181–4197.

Takahashi, H., Katayama, K., Sohya, K., Miyamoto, H., Prasad, T., Matsumoto, Y., Ota, M., Yasuda, H., Tsumoto, T., Aruga, J., et al. (2012). Selective control of inhibitory synapse development by Slitrk3-PTPdelta trans-synaptic interaction. *Nat. Neurosci.* 15, 389–398, S381–2.

Taliaferro, J.M., Vidaki, M., Oliveira, R., Olson, S., Zhan, L., Saxena, T., Wang, E.T., Graveley, B.R., Gertler, F.B., Swanson, M.S., et al. (2016). Distal alternative last exons localize mRNAs to neural projections. *Mol. Cell* 61, 821–833.

Tian, B., Hu, J., Zhang, H., and Lutz, C.S. (2005). A large-scale analysis of mRNA polyadenylation of human and mouse genes. *Nucleic Acids Res.* 33, 201–212.

Traunmuller, L., Gomez, A.M., Nguyen, T.M., and Scheiffele, P. (2016). Control of neuronal synapse specification by a highly dedicated alternative splicing program. *Science* 352, 982–986.

Tushev, G., Glock, C., Heumuller, M., Biever, A., Jovanovic, M., and Schuman, E.M. (2018). Alternative 3' UTRs modify the localization, regulatory potential, stability, and plasticity of mRNAs in neuronal compartments. *Neuron* 98, 495–511.e6.

Uemura, T., Lee, S.J., Yasumura, M., Takeuchi, T., Yoshida, T., Ra, M., Taguchi, R., Sakimura, K., and Mishina, M. (2010). Trans-synaptic interaction of GluRdelta2 and Neurexin through Cbln1 mediates synapse formation in the cerebellum. *Cell* 141, 1068–1079.

Vogel, G., and Richard, S. (2012). Emerging roles for Sam68 in adipogenesis and neuronal development. *RNA Biol.* 9, 1129–1133.

Vuong, C.K., Black, D.L., and Zheng, S. (2016). The neurogenetics of alternative splicing. *Nat. Rev. Neurosci.* 17, 265–281.

Yamagata, A., Yoshida, T., Sato, Y., Goto-Ito, S., Uemura, T., Maeda, A., Shiroshima, T., Iwasawa-Okamoto, S., Mori, H., Mishina, M., et al. (2015). Mechanisms of splicing-dependent trans-

synaptic adhesion by PTPdelta-IL1RAPL1/IL-1RAcP for synaptic differentiation. *Nat. Commun.* 6, 6926.

Yirmiya, R., Winocur, G., and Goshen, I. (2002). Brain interleukin-1 is involved in spatial memory and passive avoidance conditioning. *Neurobiol. Learn. Mem.* 78, 379–389.

Yoshida, T., Shiroshima, T., Lee, S.J., Yasumura, M., Uemura, T., Chen, X., Iwakura, Y., and Mishina, M. (2012). Interleukin-1 receptor accessory protein organizes neuronal synaptogenesis as a cell adhesion molecule. *J. Neurosci.* 32, 2588–2600.

Yoshida, T., Yasumura, M., Uemura, T., Lee, S.J., Ra, M., Taguchi, R., Iwakura, Y., and Mishina, M. (2011). IL-1 receptor accessory protein-like 1 associated with mental retardation and autism mediates synapse formation by trans-synaptic interaction with protein tyrosine phosphatase delta. *J. Neurosci.* 31, 13485–13499.

ISCI, Volume 22

Supplemental Information

SAM68-Specific Splicing Is Required for Proper Selection of Alternative 3' UTR Isoforms in the Nervous System

Yoko Iijima, Masami Tanaka, Satoko Suzuki, David Hauser, Masayuki Tanaka, Chisa Okada, Masatoshi Ito, Noriko Ayukawa, Yuji Sato, Masato Ohtsuka, Peter Scheiffele, and Takatoshi Iijima

Supplementary information

Transparent Methods

Animals All procedures related to the care and treatment of animals were carried out in strict accordance with the Guide for the Care and Use of Laboratory Animals of Tokai University. All mice were maintained under specific pathogen-free conditions at the Laboratory Animal Center, Tokai University. The experimental protocol was approved by the Institutional Animal Care and Use Committee of Tokai University (permit number 141018). All surgeries were performed under sodium pentobarbital anesthesia, with all efforts made to minimize animal suffering. **For the transcriptomic analyses, LC-MS analysis and splicing assays, we largely used more than three male animals at 2-3 months old.**

Information of animals used in this study

Animals: organism/strains	Source
Mouse: <i>Sam68/Slm1</i> double knockout: B6.129 (SJL)	Iijima et al., <i>J.Cell Biol.</i>, 2011
Mouse: <i>Slm1</i> knockout: B6.129 (SJL)	Iijima et al., <i>J.Cell Biol.</i>, 2011
Mouse: <i>Slm2</i> mutant: B6	This paper (see Figure S3)
Mouse: <i>Sam68</i> knockout: B6.129 (SJL)	Richard et al., <i>PLOS Genet.</i>, 2005

Mouse exon array Total RNA was prepared using NucleoSpin RNA XS (Takara, Japan) and quantified using a NanoDrop-1000 spectrophotometer. The quality was monitored with the Agilent 2100 Bioanalyzer (Agilent Technologies, Santa Clara, CA). One hundred nanograms of RNA was labeled with the Low Input Quick Amp WT Labeling Kit, One-Color*3 and hybridized using the SurePrint G3 Mouse Exon Microarray 2x400K (Agilent Technologies, Folsom, CA, USA) according to the manufacturer's protocol. Hybridization signals were detected using the DNA microarray scanner G2600D (Agilent Technologies), and all scanned images were analyzed using Agilent feature extraction software (v11.5.1.1). Raw data were imported with the GeneSpring GX software (v13.0, Agilent Technologies, CA, USA). After 75 percentile shift normalization, unsupervised analysis was performed by hierarchical clustering on genes and samples: Euclidean distance, and Wards linkage clustering. To locate genes that are differentially expressed in each knockout mouse group compared with WT, genes with normalized gene expression values averaged for each genotype less than -3 and raw probe signal intensity values averaged for each genotype less than 100 across three genotypes and probe's genomic coordinates located in sex chromosomes were eliminated from further analysis. We constructed scatter plots with Pearson's correlation coefficient and volcano plot conducted with moderate t-test with Benjamini-Hochberg multiple testing correction for the remaining genes. The data presented in this manuscript have been deposited in NCBI's Gene Expression Omnibus and are accessible through **GEO Series accession number GSE 110258.**

RNA-seq After the QC procedures, mRNA from eukaryotic organisms is enriched using oligo(dT) beads. For prokaryotic samples, rRNA is removed using the Ribo-Zero rRNA Removal Kit (Illumina) that leaves the mRNA. First, the mRNA is fragmented randomly by adding fragmentation buffer, then the cDNA is synthesized

using an mRNA template and random hexamer primers, after which a custom second-strand synthesis buffer (Illumina), dNTPs, RNase H, and DNA polymerase I are added to initiate the second-strand synthesis. Second, after a series of terminal repair, a ligation, and sequencing adaptor ligation, the double-stranded cDNA library is completed through size selection and PCR enrichment. The qualified libraries are fed into HiSeq PE150 sequencers (Illumina) after pooling according to the manufacturer's protocol: effective concentration and expected data volume. The filtering processes to clean reads are as follows: (1) Remove reads containing adapters. (2) Remove reads containing N > 10% (N represents the base and cannot be determined). (3) Remove reads containing low quality (Qscore <= 5) base which is over 50% of the total base. Cleaned reads were aligned to mouse reference genome mm9 with the hisat2 program (Kim et al., 2015). Aligned reads were counted in every region (gene, 5'-UTR, CDS and 3'-UTR from RefSeq mm9 version) by the featureCounts program (Liao et al., 2014). To detect the exons differentially regulated between DKO and WT, the Mixture-of-ISOforms (MISO v0.5.3) program was used. The BAM files produced by the hisat2 program and the files for alternative events for the mm9 annotation version created by rnaseqlib (<https://github.com/yarden/rnaseqlib>) were used as inputs. To identify DKO-regulated events, we used the criteria: the Bayes factor is >10. **The raw data obtained in this study can be accessed at the DDBJ database (6781), with accession number of DRA6781, with bioproject accession number of PRJDB6781.**

Antibodies and DNA constructs For immunoblot and immunostaining analyses, the following commercially available antibodies were used: mouse anti-VAMP2 (clone 69.1, Synaptic Systems, Göttingen, Germany), rabbit anti-GAPDH (G9545, Sigma-Aldrich, St Louis, MO, USA), rat anti-HA (clone 3F10, Roche Applied Science), and mouse anti-PSD-95 (1D10, Neuromab, Davis, CA, USA). Rabbit anti-SAM68, guinea pig anti-SLM1 and anti-SLM2 have been described previously (Iijima et al., 2014; Iijima et al., 2011). Secondary antibodies with minimal interspecies cross-reactivity conjugated to cyanine and Alexa 633, 546 or 488 (dyes were obtained from Jackson ImmunoResearch, Westgrove, PA, USA and Invitrogen, Carlsbad, CA, USA) were used for visualization in the immunostaining.

Expression vectors for NL1, NRX1 β , IL1PacP, IL1RAP-L1, PTP δ , Pcdh15, SLM1 and SLM2 have been previously described (Chih et al., 2006; Kazmierczak et al., 2007; Yoshida et al., 2012; Yoshida et al., 2011). For construction of expression vectors for soluble IL1PacP, soluble Pcdh15, Cp and GlyR α 3, these cDNAs were subcloned into the multi-cloning site of the pCAGGS vector.

Antibodies used in this study

Antibodies	SOURCE	IDENTIFIER
Mouse monoclonal anti-HA (clone HA-7)	Sigma-Aldrich	Product No: H9658
Mouse monoclonal anti-FLAG (M2)	Sigma-Aldrich	Product No: F1804
Rabbit polyoclocal anti-SAM68	Iijima et al., <i>Cell.</i> , 2011	N/A
Rabbit polyoclocal anti-SLM1	Iijima et al., <i>Cell.</i> , 2011	N/A

Rabbit polyclonal anti-SLM2	Iijima et al., <i>Cell.</i> , 2011	N/A
Rabbit polyclonal anti-GAPDH	Sigma-Aldrich	Product No: G9545
Mouse monoclonal anti-VAMP2 (synaptobrevin2) (clone 69.1)	Synaptic Systems	Cat#104 211
Mouse monoclonal anti-PSD95 (clone K28/43)	NeuroMab	Cat#75-028

Recombinant used in this study

Antibodies	SOURCE	IDENTIFIER
pFLAG-IL1RAcP	Yoshida et al., <i>J.Neurosci.</i> , 2012	N/A
pFLAG-IL1RAP-L1	Yoshida et al., <i>J.Neurosci.</i> , 2011	N/A
pFLAG-PTP δ	Yoshida et al., <i>J.Neurosci.</i> , 2011	N/A
pCAG Neuroligin1-HA	Chih et al., <i>Neuron</i> , 2005	N/A
pCAG Neurexin1 β -HA	Chih et al., <i>Neuron</i> , 2005	N/A
pCAG κ GRIR	Hanawa et al., <i>Mol Ther.</i> , 2002	N/A
pCAG VSVG	Hanawa et al., <i>Mol Ther.</i> , 2002	N/A
pCAG RTR2	Hanawa et al., <i>Mol Ther.</i> , 2002	N/A
pCAGGS sIL1RAP-HA	This paper	N/A
pCAGGS mPcdh15-HA	This paper	N/A
pCAGGS sPcdh15-HA	This paper	N/A
pCAGGS GlyRa3-HA	This paper	N/A
pCAGGS GlyRa3 N'ter-HA	This paper	N/A
pCAGGS mCp-HA	This paper	N/A
pCAGGS sGp-HA	This paper	N/A
pUC57-sgRNA	Addgene	Addgene No.#51132

Generation of *Slm2* mutant animals by genome editing with CRISPR/CAS9 system

All procedures were performed as described previously (Miura et al., 2015). For preparation of sgRNA and CAS9 mRNA, the sgRNA against downstream of the translation start site in exon 1 of the *Khdrbs3* gene was designed using CRISPR and CHOPCHOP (see the table below). The templates for sgRNA synthesis were PCR amplified with primer sets using pUC57-sgRNA vector (Addgene number: #51132) as

a template (see the table below). Four hundred ng of gel-purified PCR products were subjected to RNA synthesis with MEGAshortscript™ T7 Kit (Ambion) and DNase treatment followed by purification of mRNA using the MEGAclean Kit. The synthesis and purification of Cas9 mRNA was performed as described for the RNA synthesis steps of ssDNA synthesis.

For microinjection into one-cell mouse embryos, sgRNA and Cas9 mRNA were mixed (at concentrations of 14–20 ng/μl for ssDNA, 10 ng/μl for sgRNA, and 10 ng/μl for Cas9 mRNA) and co-injected into both the pronuclei and cytoplasm of C57BL6J fertilized eggs obtained using *in vitro* fertilization. Injected eggs were cultured overnight in KSOM medium at 37°C with 5% CO₂, and the resulting two-cell embryos were transferred into the oviducts of pseudo-pregnant ICR females. Oligonucleotides of the primer set for the genotyping are listed below.

Oligonucleotides for genome editing of *Khdrbs3* gene with CRISPR/CAS9 system and oligonucleotide sequences of primer sets for the genotyping

Oligos	Sequence (5'-3')
<i>Khdrbs3</i> sgRNA-F*	5'- TAA TAC GAC TCA CTA TAG G GCG CAG GGC GTG CGT GAA GG GTT TTA GAG CTA GAA ATA GCAAG -3'
sgRNA-R	5'- AAA AAA AGC ACC GAC TCG G -3'
<i>Khdrbs3</i> gt-F	5'- TAA TAC GAC TCA CTA TAG G GCG CAG GGC GTG
<i>Khdrbs3</i> gt-R	CGT GAA GG GTT TTA GAG CTA GAA ATA GCAAG -3'

*Red shows targeted sequence of *Khdrbs3* gene

RNA isolation, quantitative PCR (qPCR) and alternative-splicing assays RNA was isolated with RNAiso Plus reagent (TaKaRa, Tokyo, Japan), followed by removal of contaminating DNA using Turbo DNA-free (RNase-free DNase, Ambion, Austin, TX, USA). Two micrograms of total RNA was reverse transcribed using random hexamers and ImProm-II (Promega, Madison, WI, USA).

Quantitative PCR (qPCR) was performed on a StepOnePlus qPCR system (Applied Biosystems, Waltham, MS, USA) with Power SYBR Green PCR Master Mix (Applied Biosystems) and the comparative CT method. For the relative quantification by qRT-PCR, transcript level was normalized to that of *Gapdh*. On the other hand, the transcript levels of each splicing isoform were normalized to that of total transcripts, to avoid confounding by differences in amount of total transcripts between groups as described previously (Suzuki et al., 2017). All the oligonucleotide primer sequences used for semi-quantitative PCR and qRT-PCR are listed below. Primers for *Nrxn1/2/3* have been previously described (Iijima et al., 2011). 3'RACE was performed using the 3' RACE System for Rapid Amplification of cDNA Ends (Invitrogen, Cat#18373019). Two microliters of total RNA were used for first strand cDNA synthesis. Specific cDNA was then amplified by PCR using two gene-specific primers that anneal to a region of known exon sequences and an adapter primer that targets the poly(A) tail region.

Oligonucleotide sequences of primer sets for semi-quantitative PCR

Forward primer	Sequence	products (bp)
Reverse primer		

<i>Nrxn1</i> AS4-F	5'- TGT TGG GAC AGA TGA CAT CGC C -3'	318/228
<i>Nrxn1</i> AS4-R	5'- GAG AGC TGG CCC TGG AAG GG -3'	
<i>Nrxn2</i> AS4-F	5'- GTG CGC TTT ACT CGA AGT GGT G -3'	180/270
<i>Nrxn2</i> AS4-R	5'- CCC ATT GTA GTA GAG GCC GGA C -3'	
<i>Nrxn3</i> AS4-F	5'- TTG TGC GCT TCA CCA GGA ATG -3'	354/264
<i>Nrxn3</i> AS4-R	5'- AGA GCC CAG AGA GTT GAC CTT G-3'	
<i>Gapdh</i> -F	5'- TGT TGC CAT CAA TGA CC -3'	342
<i>Gapdh</i> -R	5'- TCT CAT GGT TCA CAC CCA -3'	
<i>Pcdh15</i> ex24-F	5'- ACC TCC TCC TGT AAG TGA GC -3'	249/318/269
<i>Pcdh15</i> ex25-R	5'- TTT GAA GGG ACT CGG AGA TTG G -3'	
<i>Pcdh15</i> ex26a-R	5'- TTT CTT CTG GAA CAC TGG -3'	
<i>Pcdh15</i> ex26b-R	5'- CAT GGT ATC ACA GAC AGA C -3'	

Oligonucleotide sequences of primer sets for RT-qPCR

Forward primer Reverse primer	Sequence	products (bp)
<i>Pcdh15</i> ex25-F <i>Pcdh15</i> ex26a-R <i>Pcdh15</i> ex26b-R	5'- CCG GGT ACA AGC AGA TTC TC -3' 5'- GGG TGA TCG TTT TCA TCC TG -3' 5'- TTG ACA CCT GGG TTC TCC AT -3'	108/101
<i>Pcdh15</i> total (ex25)-F <i>Pcdh15</i> total (ex25)-R	5'- TGG ATT ACG AGA CAA GGA CCA -3' 5'- TTG AAG GGA CTC GGA GAT TG -3'	87
<i>Cp</i> ex17-F <i>Cp</i> ex17b-R <i>Cp</i> ex19-R	5'- GCT GGG ATG GCA ACT ACC TA -3' 5'- CAG TTG TGT GGC TTG GAT TTT -3' 5'- TTT TCC TGG CTA CTC CTT GG -3'	148/149
<i>Cp</i> total-F <i>Cp</i> total-R	5'- GGT TCC TTC ACA AAC CGA AA -3' 5'- TGA ATG CTG AGA GGA TGC TG -3'	137
<i>Lrrcc1</i> ex18-F <i>Lrrcc1</i> ex19a-R <i>Lrrcc1</i> ex19b-R	5'- GCG CAC CAA GCT GAA ATA AT -3' 5'- TTG CAT GTT TCG TCC AGA AG -3' 5'- GGG TGG TGT TTT TCA GTC TCA -3'	119/111
<i>Lrrcc1</i> total (ex18)-F <i>Lrrcc1</i> total (ex18)-R	5'- TGC AAT GGA AAA GCT TCA GA -3' 5'- TCT GCT TCT CAT TTG CTA GCT G -3'	107
<i>Il1rap</i> ex8-F <i>Il1rap</i> ex9a-R <i>Il1rap</i> ex9b-R	5'- GCT GCC AAG GTG AAA CAG A -3' 5'- GGA CCA TCT CCA GCC AGT AA -3' 5'- GTG TTT TGT GTC CGA TGT GG -3'	130/127
<i>Il1rap</i> total (ex3)-F <i>Il1rap</i> total (ex3)-R	5'- ACT ACA GCA CTG CCC ATT CC -3' 5'- CGG AAC CAG AGC ACA TCT TT -3'	136
<i>Pcdh17</i> ex3a-F <i>Pcdh17</i> ex3b-R <i>Pcdh17</i> ex4-R	5'- GGG AGG CAC TCA AGA TGA AA -3' 5'- TCA GAA TGA CCA AGC ACT CG -3' 5'- TGC GAA CAG CAT TGG TAG TC -3'	109/131
<i>Pcdh17</i> total (ex3)-F <i>Pcdh17</i> total (ex3)-R	5'- CCA CGT TTA AGG ACC CAG AA -3' 5'- ATG TCA CAG CAG GAG CCT TT -3'	106
<i>Dlgap1</i> ex14-F <i>Dlgap1</i> ex14b-R <i>Dlgap1</i> ex15-R	5'- GAC ATG CTG CAG TTG TCC AT -3' 5'- TTT GTG CAG GGT TTT AAA TGG -3' 5'- CTT CTT TGG CAC TGG AGG AG -3'	149/135
<i>Dlgap1</i> total (ex14)-F <i>Dlgap1</i> total (ex14)-R	5'- TTT GGG ACA TGC TGC AGT T -3' 5'- TTG TCA AGA GGA TCC ATC TGT TT -3'	103

<i>Sema3e</i> ex17(LF)-F	5'- TGT TTG GTT ATC TTA CTG TCT TGG -3'	144
<i>Sema3e</i> ex17(LF)-R	5'- GCA ATA TGG CAC ATG CTT ACA -3'	
<i>Sema3e</i> ex17(SF)-F	5'- TGA GAA CTT CTA ATG GAT TTC TTT -3'	148
<i>Sema3e</i> ex17(SF)-R	5'- GGA TGT CAA CAT TCT CTT TAT TCA -3'	
<i>Fbxl3</i> (LF)-F	5'- TCT GTT GCC TTT GAC ATC CA -3'	124
<i>Fbxl3</i> (LF)-R	5'- TTG CTT AGG AAA CTC TAA GAA TGG -3'	
<i>Fbxl3</i> (SF)-F	5'- TCT GGA GAG ATC CGT GGA GT -3'	139
<i>Fbxl3</i> (SF)-R	5'- CCT TTA CAC ACG ATG CCT CA -3'	
<i>Glra3</i> ex4-F	5'- TGC TAA TGA GAA GGG GGC TA -3'	129/142
<i>Glra3</i> ex5a-R	5'- TTG AGA TCC ATT GGA CAG GA -3'	
<i>Glra3</i> ex5b-R	5'- AGC CAG CCA GAG TTC AGA AA -3'	
<i>Glra3</i> total(ex3)-F	5'- TCC TCC AGT TAA TGT CAC ATG C -3'	111
<i>Glra3</i> total(ex4)-R	5'- GGA TCA TTC CAC TTC TGA CGA -3'	
<i>Abhd1</i> -F	5'- TAC TCC CAA GCT CCA CTG CT -3'	124
<i>Abhd1</i> -R	5'- AAT CCC AAC ATG CAG AGG TC -3'	
<i>Padi2</i> -F (3UTR)	5'- CAG CCA TCC TCC ACC TAA AA -3'	148
<i>Padi2</i> -R (3UTR)	5'- CCT TCT CCC TTC CCT CAT TC -3'	
<i>Plac9</i> -F	5'- GTG CAA AGG CGG TTA GAC AT -3'	108
<i>Plac9</i> -R	5'- GTT TGA AGC CAG TTC CTC CA -3'	
<i>Amy1</i> -F	5'- ATC GAT GGC GTC AAA TAA GG -3'	109
<i>Amy1</i> -R	5'- CCT CTG CCA AAA GCT ACC TG -3'	
<i>Ocel1</i> -F (3UTR)	5'- GAT CAG CTA GGG CTT GAA CG -3'	112
<i>Ocel1</i> -R (3UTR)	5'- CCA GCC TTG GAA AAC AAA AA -3'	
<i>Gdpd3</i> -F	5'- GAT GGA TGA ACC AAC TGT CG -3'	106
<i>Gdpd3</i> -R	5'- AGG CAC CAA AAT AGC ACC TG -3'	
<i>Il1rapl1</i> -F	5'- CAG GAA TCA TTT TGG AGC TGA -3'	107
<i>Il1rapl1</i> -R	5'- CCC CAG TCT CTT GAT TCC AC -3'	
<i>hIL1R1</i> -F	5'- GTC TTG CCT GAG GTC TTG GA -3'	118
<i>hIL1R1</i> -R	5'- TTC TGC TTT TCT TTA CGT TTT CA -3'	
<i>PTPRD</i> -F	5'- TGA CTT CAT TGG CCA AGT CC -3'	100
<i>PTPRD</i> -R	5'- GAA AAC TCC AGT TCT TCC AAC G -3'	

Neuronal cell culture Cerebellar granule neuron cultures were prepared from ICR mouse pups on postnatal days 5–7 (P5–7). Cortical neuron cultures were prepared from ICR mouse pups on embryonic day 15 (E15). The tissues were dissociated with 0.05% trypsin (Sigma) in the presence of DNase I (Roche Applied Science) for 10 min at 37°C. After cell dissociation, trypsin was inactivated with soybean trypsin inhibitor (Sigma). Cortical neuron cultures (for RNA assays) and hippocampal neuron cultures (for calcium imaging) were prepared from ICR mouse pups using the same procedures on embryonic days 15 and 17 respectively. Cells were then plated into poly-D-lysine-coated dishes ($2.0 \times 10^5/\text{cm}^2$) and maintained for 15 days in Neurobasal Medium (Invitrogen) containing 2% B27 supplement, 2 mM Glutamax, and penicillin/streptomycin (Invitrogen). For neuron-HEK293 cell co-culture assay, HEK293T cells expressing synaptogenic molecules with GFP were plated on cerebellar granule neuron culture (DIV10–12) for 1 day ($2.0 \times 10^4/\text{cm}^2$) as described previously (Iijima et al., 2011; Sato et al., 2017). For knockdown experiments, 1–2 μM of cell permeable siRNAs (Dharmacon, Lafayette, CO; see the Table below) was

applied 5–7 days previously for harvest. Successful knockdown effects (>70%) were confirmed by RT-qPCR (data not shown).

Cell permeable siRNAs used in this study

siRNAs	SOURCE	IDENTIFIER
Human <i>Sam68</i> siRNA SMART pool	Dharmacon	E-020019-00-0005
Mouse control siRNA SMART individual	Dharmacon	D-001910-01
Mouse <i>I1rap</i> siRNA SMART pool	Dharmacon	E-042418-00-0005

Protein analysis Cells or brain tissues were lysed with RIPA buffer (25 mM Tris-HCl, pH 8.0, 150 mM NaCl, 1% NP-40, 1% deoxycholate, 0.1% SDS) containing protease inhibitor cocktail (Roche Applied Science). For protein interaction studies, the soluble fractions were subjected to immunoprecipitation for 24 h at 4°C and analyzed by immunoblotting. For visualization, HRP-conjugated secondary antibody and ECL detection (Pierce, Rockford, IL, USA) were used, with signals acquired with an image analyzer (LAS500; GE Healthcare, Milwaukee, WI, USA).

Lentivirus production The procedures of lentivirus production have been described previously (Suzuki et al., 2017). The pCL20c vectors were designed under the control of the murine stem cell virus (MSCV) promoter. The viral vector was produced by co-transfection of human embryonic kidney cells (HEK293T) with a mixture of four plasmids using a calcium phosphate precipitation method. The four-plasmid mixture consisted of 6 µg of pCAG-kGP1R, 2 µg of pCAG-4RTR2, 2 µg of pCAG-VSV-G, and 10 µg of vector plasmid pCL20c (pCL20c-MSCV-sIL1RAcP-HA-IRES-EGFP and pCL20c-MSCV-SAM68-T2A-venus). The medium containing vector particles was harvested 40 h after transfection. Medium samples were concentrated by centrifugation at 25,800 rpm for 90 min. Virus samples were then suspended in cold phosphate-buffered saline (pH 7.4), frozen in aliquots, and stored at -80°C until use. After assessing the titer in HEK293T cells, the appropriate amount of lentivirus was infected into cultured neurons 5 days before harvesting.

Ca²⁺ imaging Hippocampal neurons cultures were prepared from ICR mouse pups on embryonic days 16-17 (E16-17), and maintained for 19–22 days before calcium imaging. Neurons were loaded with intracellular Ca²⁺ sensitive fluorescent dye Fluro-4 AM (2–3 µM, AAT Bioquest, Cat#2551) for 30–40 min at 37°C in Neurobasal Medium containing 2% B27 supplement, 2 mM Glutamax, and penicillin/streptomycin. The dye solution was replaced with Neurobasal Medium not containing B27 supplement before recordings. Cultured neurons were stimulated with NMDA (20 µM, N-Methyl-D-aspartic acid, TOCRIS, Cat#0114) in the presence of IL-1β (0.01 ng/ml, PEPROTECH, Cat#211-11B). Recordings were performed using ArrayScan VTI HCS Reader (Thermo Fisher Scientific Inc., Waltham, MA, USA) at 37°C. Fluro-4 images were acquired by excitation at 475–495 nm, and emission fluorescence was collected every 1 min at 510-531 nm. Neurons were monitored for at least 4 min prior to experiments to ensure that the Ca²⁺ fluorescence was stable. For each experiment, the intensity of fluorescence at the initial time point (–4 min) was determined as a baseline. Dye influx at each time point was quantified as a fold change of the baseline. Data were analyzed using Target Activation BioApplication

version 4 (http://www.med.cam.ac.uk/wp-content/uploads/2016/02/TargetActivation_V4_LC06220800.pdf), Thermo Fisher Scientific Inc.).

Immunostaining, image acquisition, and analysis Morphometric analysis of HEK293-neuron co-culture assays was performed essentially as described (Iijima et al., 2011; Sato et al., 2017). Briefly, confocal images of GFP-positive HEK293 cells (0.40 μm optical section) were captured on a Zeiss LSM5 confocal system. The projected images were analyzed using the ImageJ software (<https://imagej.nih.gov/ij/>, National Institutes of Health: Bethesda, MD, USA). The VAMP2 or PSD95-positive area on GFP-positive HEK293 cells was measured using an optimal threshold for all images. Three independent experiments were quantitatively analyzed, and 20–30 of GFP-positive cells were quantified per group.

CLIP assay CLIP assays were performed using Magna Nuclear RIP (Cross-Linked) Nuclear RNA-Binding protein Immunoprecipitation kit (Cat. No. 17-10520, Millipore) with some modification. Adult cerebella were homogenized with PBS. After irradiation with UV light on ice (120 $\text{mJ}/\text{cm}^2 \times 2$), samples were lysed with Nuclei Isolation Buffer, and the nuclear fraction was isolated according to the protocol. Guinea pig anti-SAM68 antisera (Iijima et al., *Cell.*, 2011) or preimmune ones were used for the immunoprecipitation. The isolated RNA was reverse-transcribed and used for qPCR analysis.

Oligo-RNA pull-down experiments Thirty mers of 5'-biotinylated 2'-OMe-RNA oligonucleotides (Eurofin genomics, Tokyo, Japan) were bound to streptavidin magnetic beads (Pierce) in RP-100 buffer (20 mM HEPES pH 7.5; 1 mM dithiothreitol, 10 mM MgCl_2 , 100 mM KCl; 0.01% NP-40) overnight. The sequence of oligonucleotide was as follows; *Il1rap* 3UTR probe (PAS WT): 5'- tgt att ttc tat aat aaa gga aaa tta caa -3'; *Il1rap* 3UTR probe (PAS a/c mut): 5'- tgt att ttc tat act caa gga aaa tta caa -3'. Cleared brain lysates from P7-P10 mouse brains prepared in RIPA buffer were diluted with an equal volume of RP-100 buffer, and then incubated with the packed beads at room temperature for 1 h. Beads were washed three times with RP-100 buffer and the precipitate was subjected to immunoblot analysis. Signal intensities were quantified by ImageGauge software (Fujifilm).

Sample preparation for LC-MS analysis Hippocampal brain tissues were lysed in lysis buffer (1% sodium deoxycholate (SDC), 0.1 M TRIS, 10 mM TCEP, pH = 8.5) by homogenization with a 21G syringe followed by strong ultra-sonication (10 cycles, Bioruptor, Diagnode). After sonication sample aliquots were spun down 10min at 21000G, and the supernatant was precipitated using 20% TCA. Samples were resuspended in lysis buffer, reduced for 10 min at 95 °C and alkylated with 15 mM chloroacetamide for 30 min at 37 °C. Proteins were digested by incubation with sequencing-grade modified trypsin (1/50, w/w; Promega, Madison, Wisconsin) overnight at 37°C. To each peptide sample an aliquot of a heavy reference peptide mix containing 10 chemically synthesized proteotypic peptides (Spike-Tides, JPT, Berlin, Germany) was spiked into each sample at a concentration of 5 fmol of heavy reference peptides per 1 μg of total endogenous protein mass. Then, the peptides were cleaned up using iST cartridges (PreOmics, Munich) according to the manufacturer's instructions. Samples were dried under vacuum and stored at -80 °C until further use.

Targeted PRM-LC-MS analysis of protein isoforms

In a first step, parallel reaction-monitoring (PRM) assays (PMID: 22865924) were generated from a mixture containing 100 fmol of each heavy reference peptide and shotgun data-dependent acquisition (DDA) LC-MS/MS analysis on a Thermo Orbitrap Fusion Lumos platform (Thermo Fisher Scientific). The setup of the μ RPLC-MS system was as described previously (Pubmed-ID: 27345528). Chromatographic separation of peptides was carried out using an EASY nano-LC 1000 system (Thermo Fisher Scientific), equipped with a heated RP-HPLC column (75 μ m x 30 cm) packed in-house with 1.9 μ m C18 resin (Reprosil-AQ Pur, Dr. Maisch). Peptides were analyzed per LC-MS/MS run using a linear gradient ranging from 95% solvent A (0.15% formic acid, 2% acetonitrile) and 5% solvent B (98% acetonitrile, 2% water, 0.15% formic acid) to 45% solvent B over 60 minutes at a flow rate of 200 nl/min. Mass spectrometry analysis was performed on Thermo Orbitrap Fusion Lumos mass spectrometer equipped with a nanoelectrospray ion source (both Thermo Fisher Scientific). Each MS1 scan was followed by high-collision-dissociation (HCD) of the 10 most abundant precursor ions with dynamic exclusion for 20 seconds. Total cycle time was approximately 1 s. For MS1, 1e6 ions were accumulated in the Orbitrap cell over a maximum time of 100 ms and scanned at a resolution of 120,000 FWHM (at 200 m/z). MS2 scans were acquired at a target setting of 1e5 ions, accumulation time of 50 ms and a resolution of 30,000 FWHM (at 200 m/z). Singly charged ions and ions with unassigned charge state were excluded from triggering MS2 events. The normalized collision energy was set to 30%, the mass isolation window was set to 1.4 m/z and one microscan was acquired for each spectrum.

The acquired raw-files were database searched against a mouse database (Uniprot, download date: 2017/04/18, total of 34,490 entries) by the MaxQuant software (Version 1.0.13.13). The search criteria were set as following: full tryptic specificity was required (cleavage after lysine or arginine residues); 3 missed cleavages were allowed; carbamidomethylation (C) was set as fixed modification; Arg10 (R), Lys8 (K) and oxidation (M) as variable modification. The mass tolerance was set to 10 ppm for precursor ions and 0.02 Da for fragment ions. The best 6 transitions for each peptide were selected automatically using an in-house software tool and imported to Skyline (version 4.1 (<https://brendanx-uw1.gs.washington.edu/labkey/project/home/software/Skyline/begin.view>)). A mass isolation lists containing all selected peptide ion masses were exported from Skyline and imported into the Lumos operating software for PRM analysis using the following settings: The resolution of the orbitrap was set to 120k FWHM (at 200 m/z) and the fill time was set to 246 ms to reach a target value of 1e6 ions. Ion isolation window was set to 0.4 Th and the scan range was set to 150-1500 Th. A MS1 scan using the same conditions as for DDA was included in each MS cycle. Each condition was analyzed in biological quintuplicates. All raw-files were imported into Skyline for protein / peptide quantification. To control for variation in sample amounts, the total ion chromatogram (only comprising peptide ions with two or more charges) of each sample was determined by Progenesis Q1 (version 2.0, Waters) and used for normalization.

Heavy-labelled reference peptide sequences used for PRM

Isoform	Peptide #1	Peptide #2
Isoform 1/2/3 (total)	<i>VAFPLEVVQK</i>	<i>NYVCHAR</i>
Isoform 1	<i>TVLTVIK</i>	<i>AGLENMASR</i>

Statistical analysis GraphPad Prism 5 (<http://www.graphpad.com/scientific-software/prism/>, GraphPad Software, Inc., San Diego, CA, USA) was used for the statistical analysis. Pairwise comparisons were performed using Student's t-test. For multiple comparisons, analysis of variance (ANOVA) followed by Bonferroni's or Dunnett's test was used.

The statistical analysis (ANOVA, Welch t tests, false discovery rate correction) and graph creations of mouse exon microarray and RNA sequencing data were performed with the R software (<https://www.r-project.org/>, Vienna, Austria) or GeneSpring GX software (<https://www.agilent.com/en/products/software-informatics/life-sciences-informatics/genespring-gx>, v13.0, Agilent Technologies) Data are represented as the mean \pm SEM. Significance is indicated as follows: ***, $p < 0.001$; **, $p < 0.01$; *, $p < 0.01$.

Supplementary References

- Chih, B., Gollan, L., and Scheiffele, P. (2006). Alternative splicing controls selective trans-synaptic interactions of the neuroligin-neurexin complex. *Neuron* 51, 171-178.
- Ehrmann, I., Dalglish, C., Liu, Y., Danilenko, M., Crosier, M., Overman, L., Arthur, H.M., Lindsay, S., Clowry, G.J., Venables, J.P., *et al.* (2013). The tissue-specific RNA binding protein T-STAR controls regional splicing patterns of neurexin pre-mRNAs in the brain. *PLoS Genet* 9, e1003474.
- Iijima, T., Iijima, Y., Witte, H., and Scheiffele, P. (2014). Neuronal cell type-specific alternative splicing is regulated by the KH domain protein SLM1. *J Cell Biol* 204, 331-342.
- Iijima, T., Wu, K., Witte, H., Hanno-Iijima, Y., Glatter, T., Richard, S., and Scheiffele, P. (2011). SAM68 regulates neuronal activity-dependent alternative splicing of neurexin-1. *Cell* 147, 1601-1614.
- Kazmierczak, P., Sakaguchi, H., Tokita, J., Wilson-Kubalek, E.M., Milligan, R.A., Muller, U., and Kachar, B. (2007). Cadherin 23 and protocadherin 15 interact to form tip-link filaments in sensory hair cells. *Nature* 449, 87-91.
- Kim, D., Langmead, B., and Salzberg, S.L. (2015). HISAT: a fast spliced aligner with low memory requirements. *Nat Methods* 12, 357-360.
- Liao, Y., Smyth, G.K., and Shi, W. (2014). featureCounts: an efficient general purpose program for assigning sequence reads to genomic features. *Bioinformatics* 30, 923-930.
- Miura, H., Gurumurthy, C.B., Sato, T., Sato, M., and Ohtsuka, M. (2015). CRISPR/Cas9-based generation of knockdown mice by intronic insertion of artificial microRNA using longer single-stranded DNA. *Sci Rep* 5, 12799.
- Sato, Y., Suzuki, S., Iijima, Y., and Iijima, T. (2017). Neuroligin-induced presynaptic differentiation through SLM2-mediated splicing modifications of neurexin in cerebellar cultures. *Biochem Biophys Res Commun* 493, 1030-1036.
- Suzuki, S., Ayukawa, N., Okada, C., Tanaka, M., Takekoshi, S., Iijima, Y., and Iijima, T. (2017). Spatio-temporal and dynamic regulation of neurofascin alternative splicing in mouse cerebellar neurons. *Sci Rep* 7, 11405.

Traunmuller, L., Bornmann, C., and Scheiffele, P. (2014). Alternative splicing coupled nonsense-mediated decay generates neuronal cell type-specific expression of SLM proteins. *J Neurosci* 34, 16755-16761.

Traunmuller, L., Gomez, A.M., Nguyen, T.M., and Scheiffele, P. (2016). Control of neuronal synapse specification by a highly dedicated alternative splicing program. *Science* 352, 982-986.

Yoshida, T., Shiroshima, T., Lee, S.J., Yasumura, M., Uemura, T., Chen, X., Iwakura, Y., and Mishina, M. (2012). Interleukin-1 receptor accessory protein organizes neuronal synaptogenesis as a cell adhesion molecule. *J Neurosci* 32, 2588-2600.

Yoshida, T., Yasumura, M., Uemura, T., Lee, S.J., Ra, M., Taguchi, R., Iwakura, Y., and Mishina, M. (2011). IL-1 receptor accessory protein-like 1 associated with mental retardation and autism mediates synapse formation by trans-synaptic interaction with protein tyrosine phosphatase delta. *J Neurosci* 31, 13485-13499.

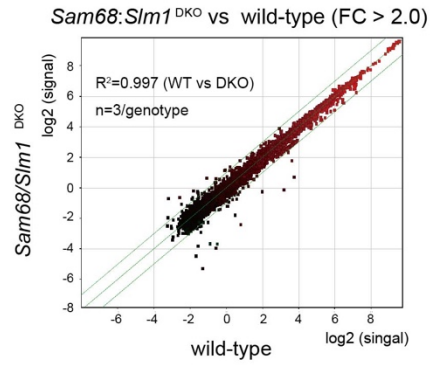
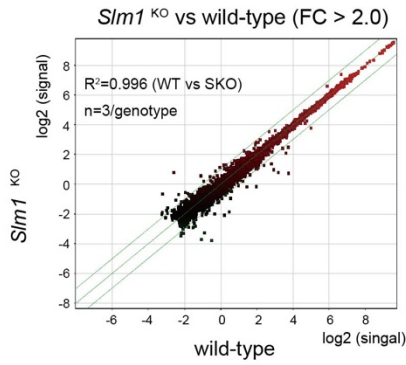
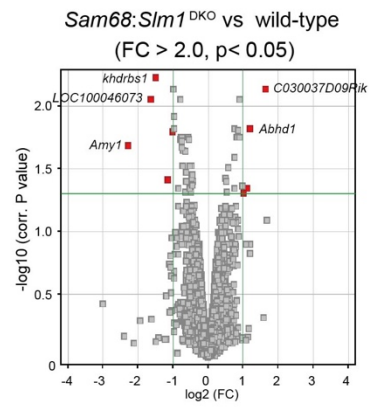
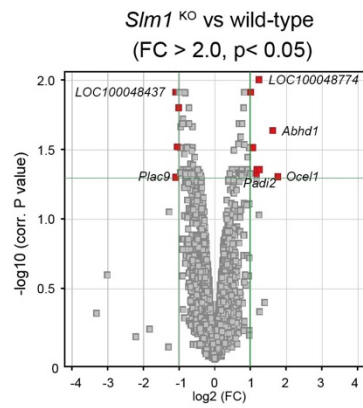
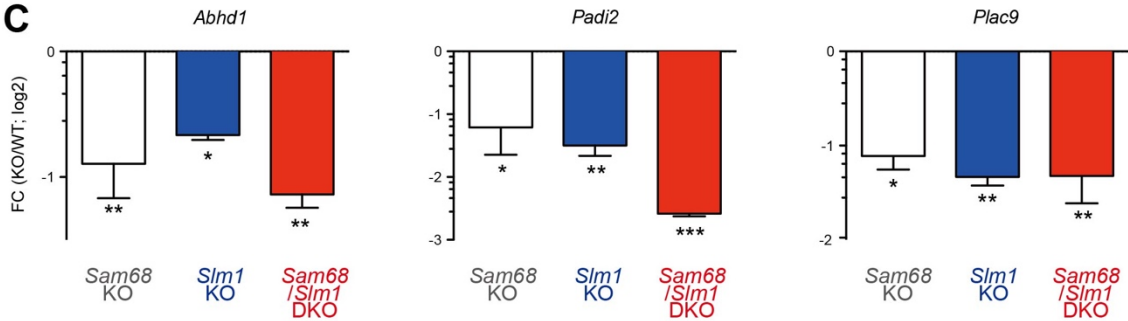
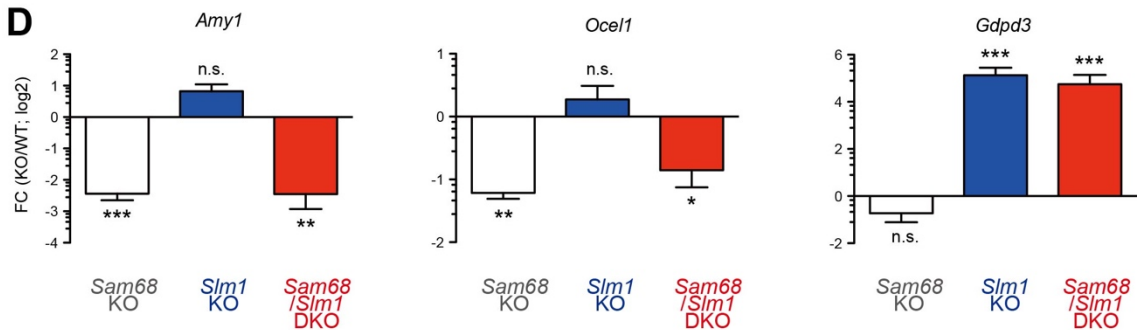
A**B****C****D**

Figure S1: Gene expression profiles in *Sam68*^{KO} and *Sam68/Slm1*^{DKO} brains, related to Figure 1

Total RNAs from midbrains of WT, *Slm1*^{KO}, and *Sam68/Slm1*^{DKO} mice were subjected to data analyses on exon array (Agilent, Sure Print G3 Mouse Exon Microarray 2x400K) (n=3 animals/genotype).

(A) Scatter plots of fold change for gene expression (*Sam68/Slm1*^{DKO} vs WT, *Slm1*^{KO} vs WT) (total 18,810 genes; threshold set: normalized gene expression >-3 in either of the two genotypes).

(B) Volcano plots showing fold change and p-values for genes shown in (A). Red shows genes that significantly changed by >two-fold (*Sam68/Slm1*^{DKO} vs WT, *Slm1*^{KO} vs WT, *Sam68/Slm1*^{DKO} vs *Slm1*^{KO}; threshold set: FC ≥ 2.0, normalized gene expression >-3 in either of the two genotypes, p-value<0.05).

(C,D) Validation of altered by RT-qPCR analysis using adult midbrains from WT, *Sam68*^{KO}, *Slm1*^{KO}, and *Sam68/Slm1*^{DKO} mice. Fold change (FC) and significant differences were compared to WT mice. Whereas the CT value of these transcripts was normalized to that of *Gapdh*. (C) Altered genes shared between *Sam68*^{KO} and *Slm1*^{KO}. (D) Altered genes unique for *Sam68*^{KO} or *Slm1*^{KO}.

Data are presented as the mean ± SEM. Significance is indicated as follows: ***, p<0.001; **, p<0.01; *, p<0.05. student's t-test.

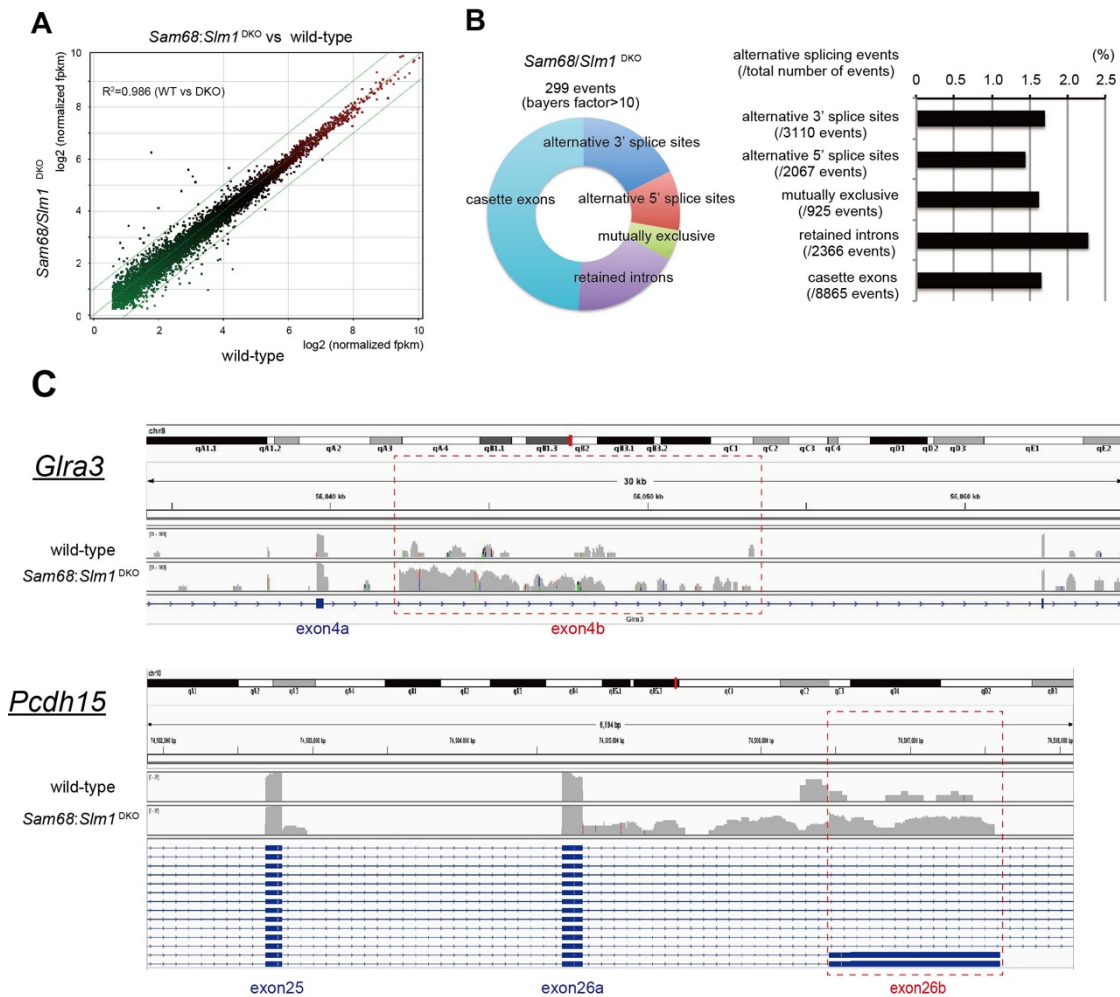


Figure S2: Analyses by RNA-sequencing, related to Figures 1 and 2

(A) Scatter plots of fold change (≥ 2.0) for gene expression (*Sam68/Slm1*^{DKO} vs WT). Expression level was measured by fragments per kilobase of mRNA per million mapped reads (fpkm) (Filtrations: ≥ 10 reads; fpkm values ≥ 50 in 2 of 2 samples).

(B) Classification of alternative splicing events by the exon junction read in wild-type and *Sam68/Slm1*^{DKO} mice using the MISO software. The pie chart shows the percentage of five types of alternative exon changes (i.e., cassette exons, mutually exclusive exons, tandem cassette exons, alternative 5'-site, alternative 3'-site, and intron retention) in the *Sam68/Slm1*^{DKO} midbrain. The graph shows the relative ratio of altered splicing events to total events.

(C) Aberrant ALE choice of *Pcdh15* and *Gla3* in *Sam68/Slm1*^{DKO} brains shown in RNA-seq. Data were based on the UCSC genome browser Mouse NCBI37/mm10 assembly.

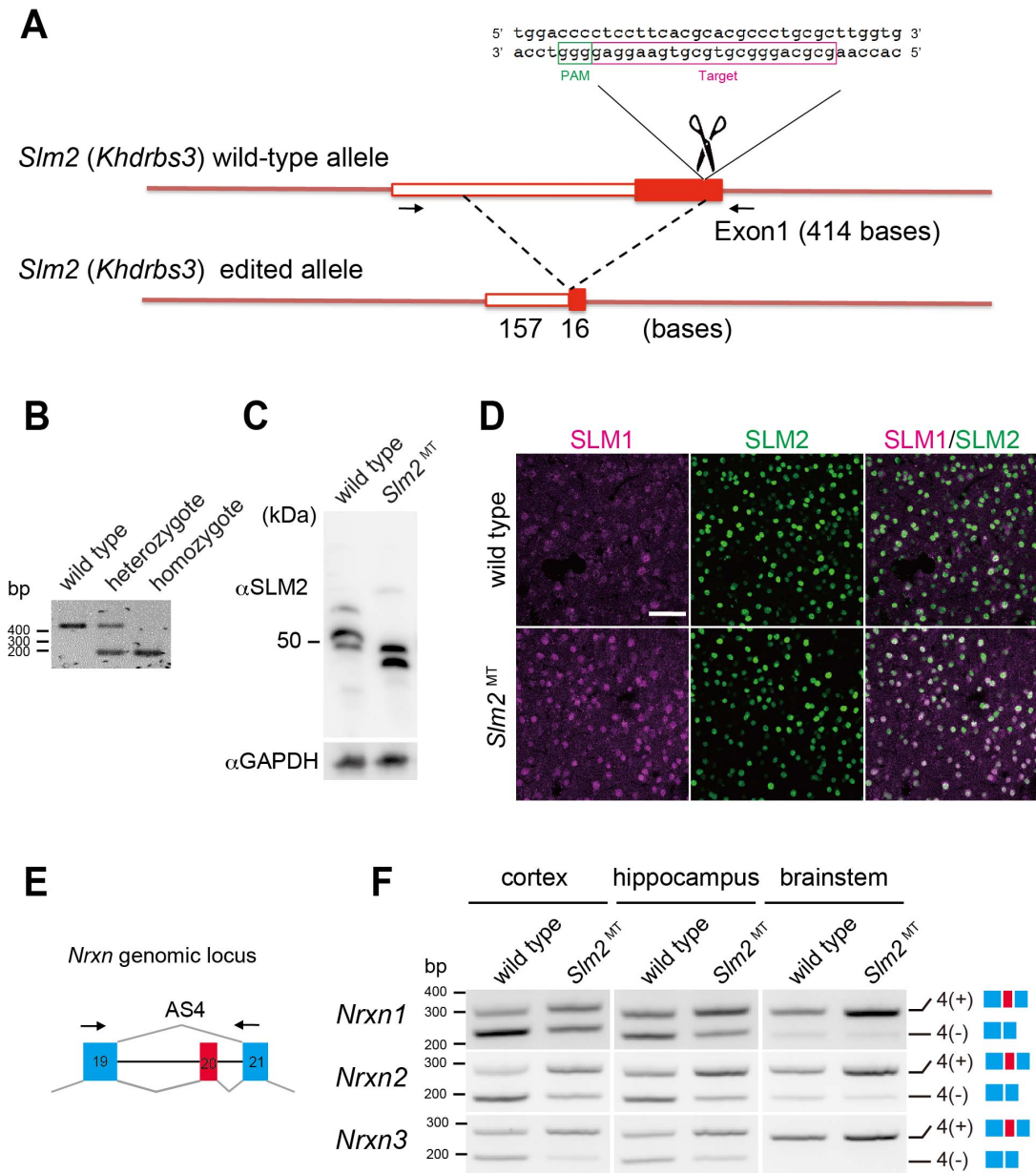


Figure S3: Generation of *Slm2* mutant (*Slm2*^{MT}) mice by genome editing, related to Figure 3

(A) Illustration of *Slm2* (*Khdrbs3*) gene disruption by genome editing with the CRISPR /CAS9 system.

(B) Images of genotyping of *Slm2*^{MT} mice by genomic PCR. Positions of the primer are shown with arrows in (A).

(C) Representative images of western blot analysis with the α-SLM2 antibody. Whereas more than 50 kDa of SLM2 protein was expressed in wild-type's brains, approximately 40 kDa of

SLM2 proteins lacking a first QUA domain with alternative methionine start codon were detected in *Slm2*^{MT} mice.

(D) Co-immunohistochemistry with α -SLM1 and α -SLM2 antibodies in the cerebral cortex. *Slm2*^{MT} mice exhibited strong immunoreactivity for SLM2 comparable to that in wild-type mice. Consistent with a previous report that SLM1 protein level was ectopically upregulated by loss-of-function of SLM2 (Traunmuller et al., 2014), immunoreactivity for SLM1 was enhanced in the mutant mice. Scale bar = 50 μ m.

(E) Representative images of semi-quantitative RT-PCR with *Nrxn1-3* AS4 performed on the cortex, hippocampus, and brainstem from wild-type and *Slm2*^{MT} mice. Similar to *Slm2*^{KO} mice previously reported (Ehrmann et al., 2013; Traunmuller et al., 2016), skipping of exon 20 in all the *Nrxns* was dramatically impaired in the mutant mice.

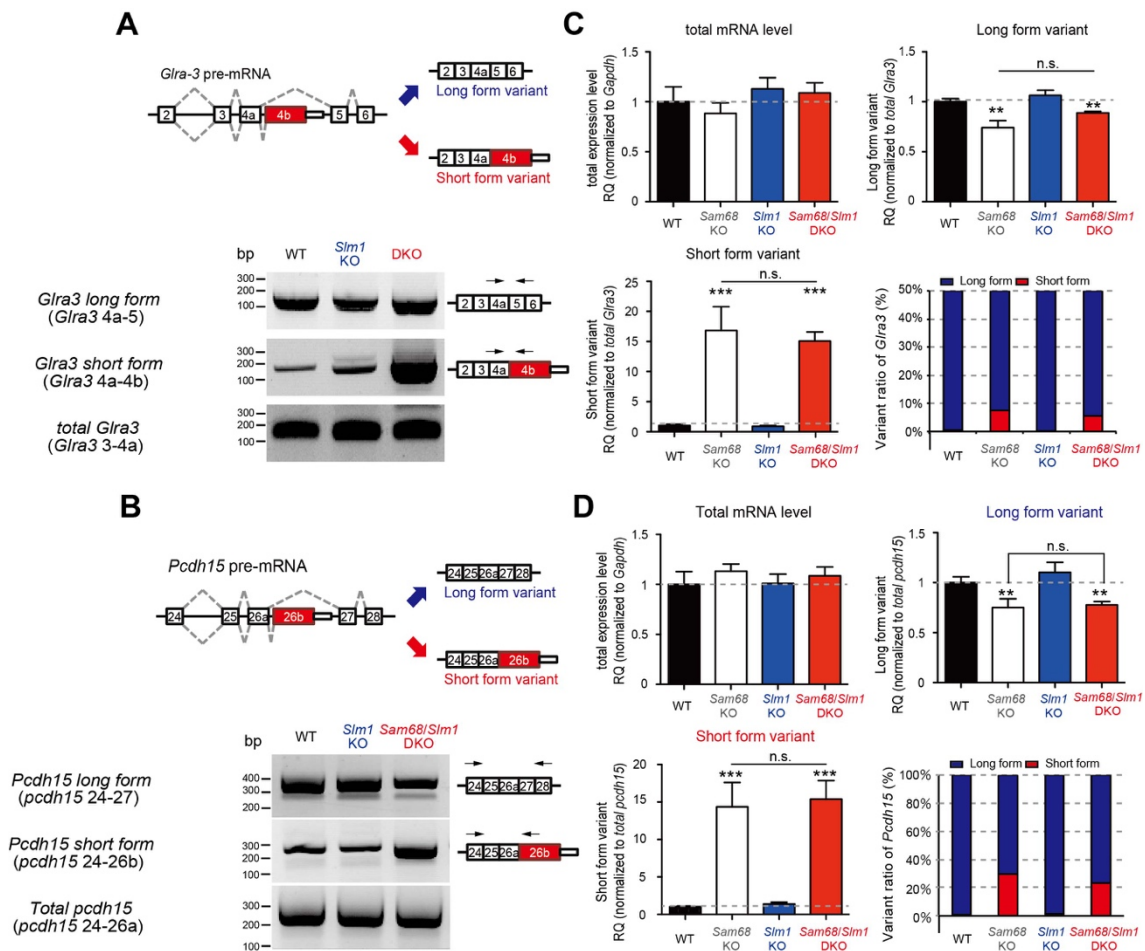


Figure S4: Appearance of atypical soluble isoforms of *Gira3* and *Pcdh15* in *Sam68*^{KO} brains by aberrant ALE usage, related to Figure 4

(A, B) Schematic illustration of alternative exon choice at *Gira3* exon 4 and *Pcdh15* exon 13 (top panel) the representative gel images of semi-quantitative RT-PCR with the 3'UTR exon choice in midbrains from wild-type, *Slm1*^{KO}, and *Sam68/Slm1*^{DKO} mice (bottom panel). (C, D) Relative levels of total mRNA and two alternative isoforms [long form variant (LF) and short form variant (SF)] and abundance ratio of SF (Red) to LF (Blue) between midbrains from wild-type, *Sam68*^{KO}, *Slm1*^{KO}, and *Sam68/Slm1*^{DKO} mice by qRT-PCR. Whereas the RQ value of total transcripts was normalized to that of *Gapdh*, the RQ value of each alternative isoform was normalized to that of total mRNA. For the abundance ratio of SF to LF, the percentage of the SF variant was largely estimated from the CT value (C_T^{SF}) directly compared to that of LF (C_T^{LF}) at the same threshold set for the CT value. $RQ^{LF} + RQ^{SF}$ values were set to 100% (n=3 animals per each genotype).

Data are presented as the mean \pm SEM. Significance is indicated as follows: **, p<0.01; *, p<0.05. One-way ANOVA followed by Dunnett's test.

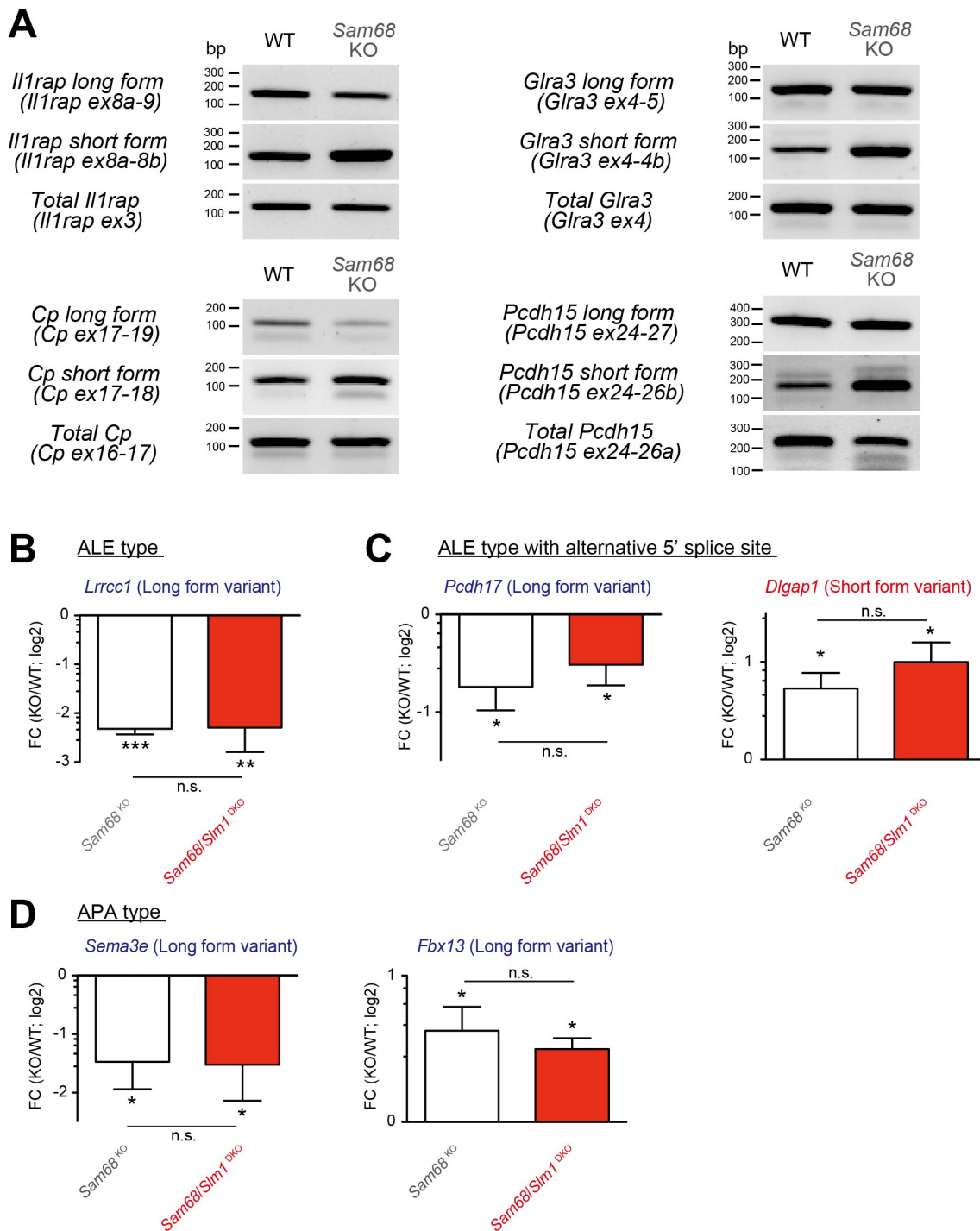


Figure S5: Altered 3'UTR isoform choice in *Sam68*^{KO} brains, related to Figure 3 and 4
 (A) Representative gel images of semi-quantitative RT-PCR with the 3'UTR exon choice in midbrains from wild-type and *Sam68*^{KO} mice.
 (B-D) No additive effects of aberrant 3'UTR isoform selections between *Sam68*^{KO} and

Sam68/Slim1^{DKO} mice. Fold change (FC) and significant difference was compared to WT. Statistical differences were further tested between *Sam68*^{KO} and *Sam68/Slim1*^{DKO} mice to exclude any additive or synergetic effect of *Sam68* and *Slim1* knock out. Each alternative isoform was normalized to that of each total mRNA. (n=3–6 animals per genotype) (B) ALE type. Long form variant of *Lrrcc1* (leucine-rich repeat and coiled-coil domain-containing protein 1). (C) ALE type with alternative 5' splice sites. Two genes, short form variant of *Dlgap1* (disk large-associated protein 1) and long form variant of *Pcdh17* (protocadherin 17). (D) APA type. Two genes, long form variant of *Fbxl3* (F-box/LRR-repeat protein3) and long form variant of *Sema3e* (semaphorin 3e).

Data are presented as the mean \pm SEM. Significance is indicated as follows: **, p<0.01; *, p<0.05. One-way ANOVA followed by Dunnett's test.

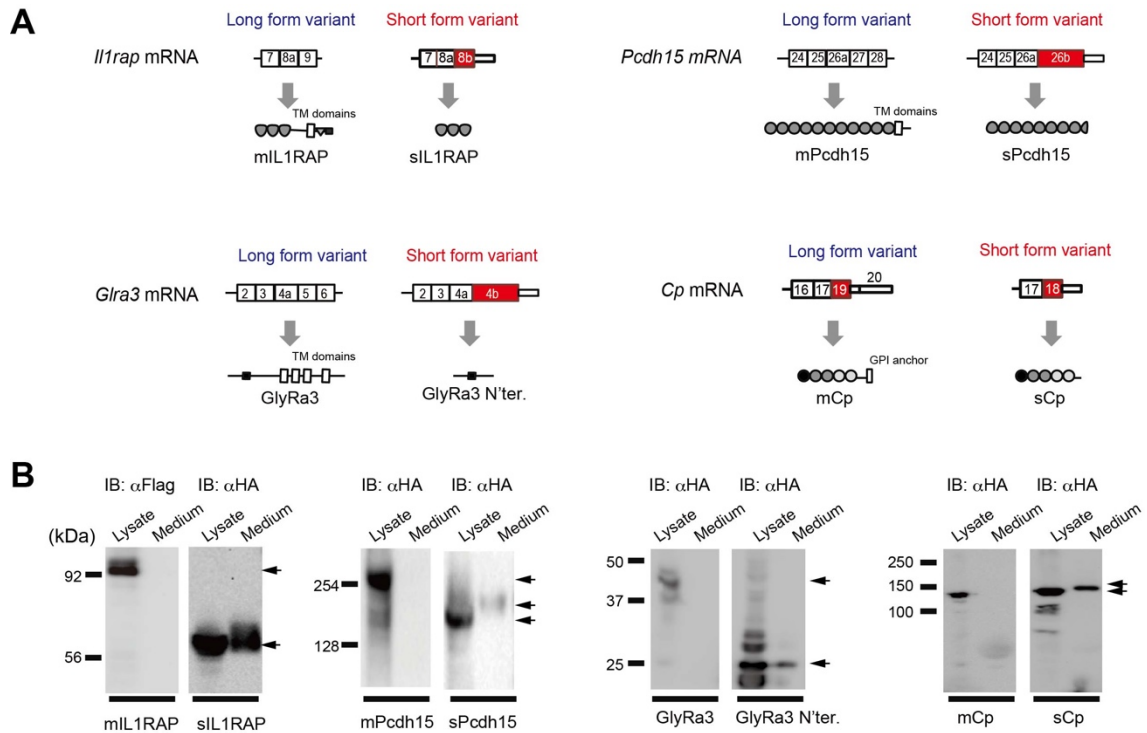


Figure S6: Secretion properties of the soluble isoforms of IL1RAP, GlyRa3, and Pcdh-15, related to Figure 4

(A) ALE choice of *Il1rap*, *Cp*, *Glra3*, and *Pcdh15* produces two types of protein products, a membrane-bound type and a soluble one.

(B) Western blot analysis using lysates of HEK293 cells expressing the soluble forms. Both membrane and soluble proteins (HA or FLAG-tagged recombinant proteins) were respectively expressed into HEK293T cells with the transfection, and cells were harvested 2 days after the transfection. Significant amounts of the soluble isoforms were released into the cultured medium.

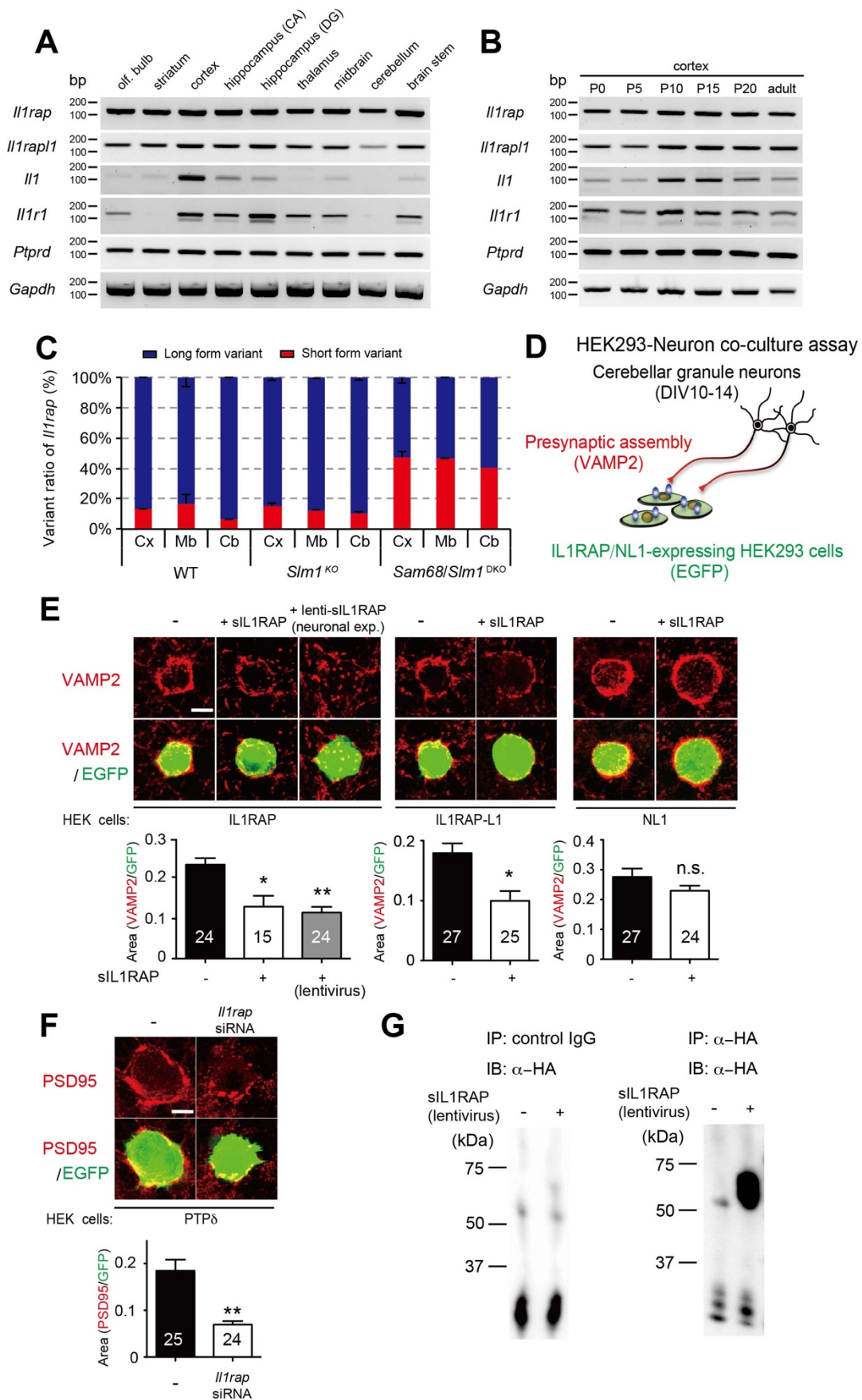


Figure S7: Soluble IL1RAP disturbs PTP δ -induced synaptogenic signaling, related to Figure 5

(A, B) Expression of *Il1rap* and the related gene transcripts (*Il1rapl1*, *Il1*, *Il1r1*, and *Ptprd*) in the central nervous system by semiquantitative RT-PCR. (A) Various brain regions. (B) Developing cortex.

(C) Abundance ratio of *Il1rap* SF to LF between midbrains from wild-type, *Slm1*^{KO}, and *Sam68/Slm1*^{DKO} mice in three brain regions, cortex (Cx), midbrain (Mb), and cerebellum (Cb).

(D) Schematic illustration of neuron-HEK293T cell co-culture assay. To examine IL1RAP-mediated presynaptic assembly, HEK293T cells expressing IL1RAP or neuroligin1 (NL1)-HA were co-cultured with cerebellar neurons (DIV10-14).

(E) Co-cultures of cerebellar granule neurons and HEK293T cells. Presynaptic assembly on HEK293T cells was detected by immunostaining with the presynaptic marker synaptobrevin (VAMP2). The overall morphology of co-cultured HEK293T cells was visualized with GFP. HEK293T cells expressing IL1RAP-FLAG, IL1RAP-L1-FLAG, or neuroligin-1 (NL1)-HA with or without sIL1RAP-HA (plasmid ratio 1:1). Further, HEK293T cells expressing IL1RAP were co-cultured with cerebellar granule neurons expressing sIL1RAP-HA with lentiviral infection (n=15–27 cells per group in >10 of separated fields [see the number on each graph column]). Scale bar=5 μ m.

(F) HEK293T cells expressing PTP δ were cocultured with control or IL1RAP knockdown neurons, and then immunostained with a post-synapse marker, anti-PSD-95 antibody.

(G) Detection of sIL1RAP-HA in the condition medium from cortical neuron culture by immunoprecipitation analysis with anti-HA antibody. sIL1RAP-HA was not immunoprecipitated with control IgG.

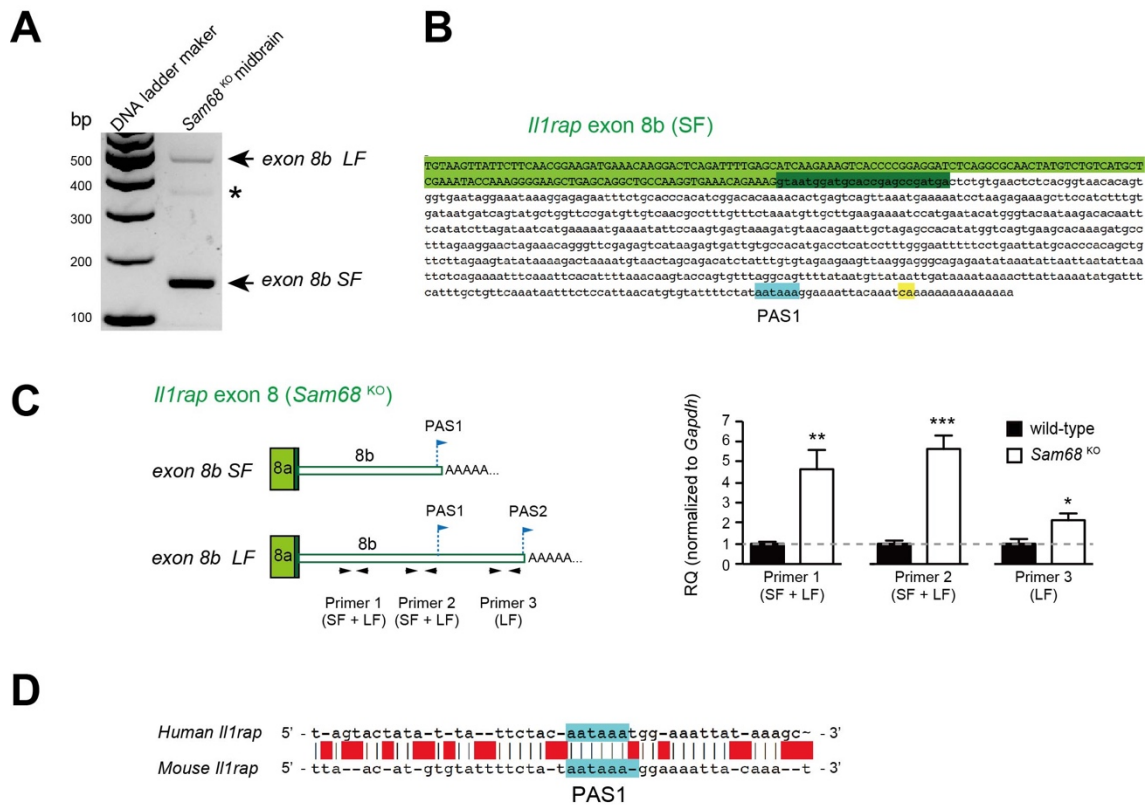


Figure S8: Identification of SAM68 recognition element in intron 8 of *Il1rap*, related to Figure 6

(A) Gel loading image of the 3'RACE assay from *Sam68*^{KO} mice. Arrows show two transcripts of *Il1rap* short isoforms. The upper band is the transcript encoding the full-length of *Il1rap* exon 8b (exon 8b LF). The lower band is the one lacking approximately 400 bp of the 3'end sequence (exon 8b SF). The asterisk denotes an unspecific PCR product.

(B) The cDNA sequence of *Il1rap* exon 8 SF. Green indicates the coding exon region. Blue shows the putative PAS site (PAS1) on the exon 8b SF UTR. Yellow shows the putative cleavage site.

(C) Survey of the 3'UTR length of *Il1rap* exon 8b by RT-qPCR analysis. Arrowheads show the positions of primer sets. The amount of these PCR products in *Sam68*^{KO} brains was compared to wild-type ones. All the products were significantly detectable in *Sam68*^{KO} brains compared to wild-type (n=5). RQ values for wild-type brain were set to 1.0.

(D) Conserved PAS1 sequence between humans and mice. Blue shows the PAS1 sequence. Data are presented as the mean \pm SEM. Significance is indicated as follows: ***, p<0.001; **, p<0.01; *, p<0.05. student's t-test.

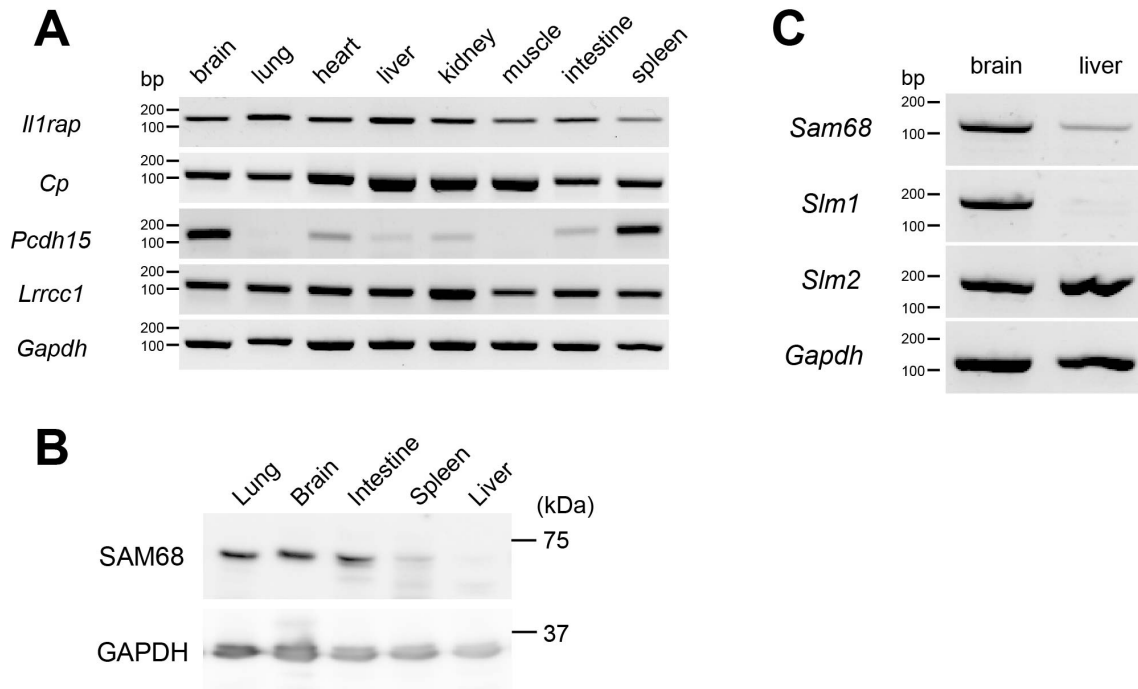


Figure S9: Tissue-specific splicing of ALEs of *Il1rap*, related to Figure 7

(A) Expression of *Il1rap*, *Cp*, *Pcdh15*, and *Lrrcc1* transcripts in various tissues by semiquantitative RT-PCR.

(B) Abundance of SAM68 protein in five tissues: brain, liver, intestine, lung, and spleen. Western blot analysis using total lysate from five tissues was performed with rabbit α -SAM68 antibody.

(C) Expression of *Sam68*, *Slm1*, and *Slm2* transcripts between the brain and liver by semiquantitative RT-PCR.